


FULL PAPER

Open Access



The influence of anisotropic electrical resistivity on surface magnetotelluric responses and the design of two new anisotropic inversions

Wisart Thongyoy¹, Weerachai Siripunvaraporn^{1,2}, Tawat Rung-Arunwan³ and Puwis Amatyakul^{1,2*} 

Abstract

Using the 3-D axial anisotropy, the dipping anisotropy, and the azimuthal anisotropy as case studies, we investigated the influence of each anisotropic resistivity element on the magnetotelluric surface responses. To justify the strong and weak influence and edge effect, we have introduced the influence indices for the impedance components, and the edge effect indices for the tipper components. Interestingly, for decoupled modes, we found that ρ_{xx} has a strong influence on Z_{xy} , Z_{yy} , and T_y , while ρ_{yy} strongly affects Z_{yx} , Z_{xx} , and T_x . The three elements ρ_{zz} , ρ_{xz} , and ρ_{yz} have only a very weak influence on all types of responses. For the coupled mode, ρ_{xx} , ρ_{yy} , and ρ_{xy} display a strong influence on all responses. Based on our studies on the influence of the anisotropic resistivity elements, we design and propose two practical processes to replace the conventional axial, dipping, azimuthal, and general anisotropic inversions. First, the axial or dipping inversion can be approximately decoupled into ρ_x -mode and ρ_y -mode inversions. The decoupled mode inversions can be performed either independently and in parallel, or as a joint inversion. Second, since the three resistivity elements always show a weak influence, the general anisotropic inversion can be simplified to just the reduced coupled azimuthal anisotropic inversion with only three resistivity elements as outputs. Both proposed techniques can save a lot of the computational resources. Criteria to choose either the decoupled or coupled modes depend greatly on the magnitudes and distributions of the Z_{xx} and/or Z_{yy} and T_x and/or T_y responses.

*Correspondence:

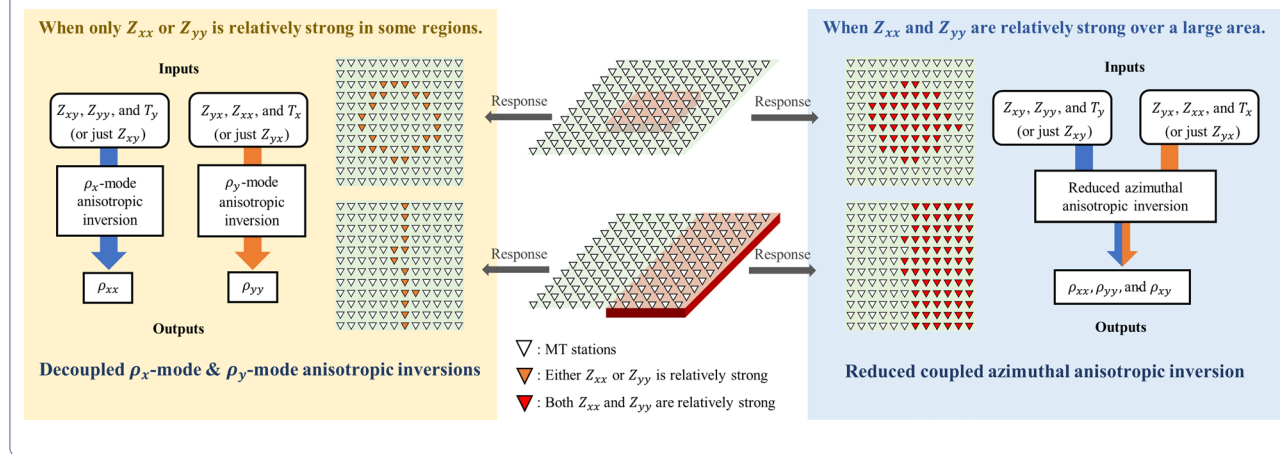
Puwis Amatyakul
puwis.mahidol@gmail.com

Full list of author information is available at the end of the article



© The Author(s) 2023. **Open Access** This article is licensed under a Creative Commons Attribution 4.0 International License, which permits use, sharing, adaptation, distribution and reproduction in any medium or format, as long as you give appropriate credit to the original author(s) and the source, provide a link to the Creative Commons licence, and indicate if changes were made. The images or other third party material in this article are included in the article's Creative Commons licence, unless indicated otherwise in a credit line to the material. If material is not included in the article's Creative Commons licence and your intended use is not permitted by statutory regulation or exceeds the permitted use, you will need to obtain permission directly from the copyright holder. To view a copy of this licence, visit <http://creativecommons.org/licenses/by/4.0/>.

Graphical Abstract



Introduction

In the past few decades, many magnetotelluric (MT) surveys have confirmed the existence of electrical anisotropy in both the crust and upper mantle both in land and marine environments (Häuserer and Junge 2011; Liddell et al. 2016; Kirkby et al. 2016; Matsuno and Evans 2017; Feucht et al. 2017, 2019; Bedrosian et al. 2019; Kirkby and Duan 2019; Liu et al. 2019; Miller et al. 2019; Ye et al. 2019; Comeau et al. 2020; Matsuno et al. 2020; Segovia et al. 2021; Rong et al. 2022). Many studies show that performing an isotropic inversion on the observed anisotropic data can lead to misinterpretation due to many inversion artifacts appearing in the inverted model (e.g., Miensoopust and Jones 2011; Häuserer and Junge 2011; Löwer and Junge 2017; Wang et al. 2017; Cao et al. 2018; Luo et al. 2020; Rong et al. 2022). There is therefore a great demand for 3-D anisotropic inversion code. Even though much 3-D anisotropic forward codes have been developed in the past decade (e.g., Jaysaval et al. 2016; Löwer and Junge 2017; Wang et al. 2017; Han et al. 2018; Liu et al. 2018; Yu et al. 2018; Cao et al. 2018; Kong et al. 2018; Rivera-Rios et al. 2019; Xiao et al. 2019; Guo et al. 2020; Luo et al. 2020; Ye et al. 2021; Bai et al. 2022), development of 3-D anisotropic inversion code to successfully invert observed MT data to obtain a more reasonable interpretation is still ongoing (Wang et al. 2017; Cao et al. 2018, 2021; Luo et al. 2020; Kong et al. 2021; Rong et al. 2022).

With an aim in the future to reach a reasonable design for a quality 3-D anisotropic inversion, we must first understand how each anisotropic resistivity element influences the surface responses. A stronger influence means that different values of the resistivity element

provide distinct response magnitudes. For example, the isotropic resistivity at a reasonable depth has a very strong influence on most MT responses which is why 3-D isotropic inversion can be accomplished (e.g., Siripunvaraporn et al. 2005; Siripunvaraporn and Egbert 2009; Siripunvaraporn and Sarakorn 2011; Siripunvaraporn 2012; among many others). In contrast, for a weak influence element, a large range of resistivity values can yield similar response magnitudes. For example, a small 3-D isotropic resistivity body located at greater depth can have a very weak influence resulting in the failure of the inversion process to recover these small structures. Since the influence is a major factor controlling the success or failure of the anisotropic inversion, our main goal in this paper is to study the influence of each anisotropic resistivity element on the surface responses in many different aspects. At the end, we recommend two new methods for 3-D anisotropic inversion to replace the general or axial anisotropic inversion.

In an isotropic media, the electrical resistivity ρ is a scalar. In the presence of a macroscopic anisotropy, the direction-dependent electrical resistivity of the medium must be defined as the tensor,

$$\boldsymbol{\rho} = \begin{bmatrix} \rho_{xx} & \rho_{xy} & \rho_{xz} \\ \rho_{yx} & \rho_{yy} & \rho_{yz} \\ \rho_{zx} & \rho_{zy} & \rho_{zz} \end{bmatrix}, \quad (1)$$

where x points north, y points east, and z points downward. The resistivity tensor is symmetric and positive definite. It can also be represented by the axial anisotropic resistivity, $\hat{\rho} = \begin{bmatrix} \rho_x & 0 & 0 \\ 0 & \rho_y & 0 \\ 0 & 0 & \rho_z \end{bmatrix}$, and their correspond-

ing rotational angles: α_S , the anisotropic strike angle, α_D , the anisotropic dipping angle, and α_L , the anisotropic slant angle (see Pek and Santos (2002) for illustration of these angles). Then,

$$\rho = \mathbf{R}_z^T(\alpha_S) \mathbf{R}_x^T(\alpha_D) \mathbf{R}_z^T(\alpha_L) \hat{\rho} \mathbf{R}_z(\alpha_L) \mathbf{R}_x(\alpha_D) \mathbf{R}_z(\alpha_S), \quad (2)$$

$$\text{where } \mathbf{R}_z(\theta) = \begin{bmatrix} \cos\theta & \sin\theta & 0 \\ -\sin\theta & \cos\theta & 0 \\ 0 & 0 & 1 \end{bmatrix}, \text{ and } \mathbf{R}_x(\theta) = \begin{bmatrix} 1 & 0 & 0 \\ 0 & \cos\theta & \sin\theta \\ 0 & -\sin\theta & \cos\theta \end{bmatrix}.$$

Besides the axial resistivity anisotropy, there are also other cases generated from the \mathbf{R}_z and \mathbf{R}_x rotational

matrices, like the azimuthal anisotropy, $\begin{bmatrix} \rho_{xx} & \rho_{xy} & 0 \\ \rho_{yx} & \rho_{yy} & 0 \\ 0 & 0 & \rho_{zz} \end{bmatrix}$,

resulting from $\mathbf{R}_z^T(\theta) \hat{\rho} \mathbf{R}_z(\theta)$, and the dipping anisotropy,

$$\begin{bmatrix} \rho_{xx} & 0 & 0 \\ 0 & \rho_{yy} & \rho_{yz} \\ 0 & \rho_{zy} & \rho_{zz} \end{bmatrix}, \text{ resulting from } \mathbf{R}_x^T(\theta) \hat{\rho} \mathbf{R}_x(\theta). \text{ These axial,}$$

azimuthal, and dipping anisotropies will be the subject of our studies in later sections.

Each of these elements has shown a different influence on the two types of MT responses: the complex impedance tensor $\mathbf{Z} = \begin{bmatrix} Z_{xx} & Z_{xy} \\ Z_{yx} & Z_{yy} \end{bmatrix}$ and the vertical magnetic transfer function or tipper $\mathbf{T} = [T_x \ T_y]$. Past studies (Yin 2003; Pek and Santos 2002; Pek and Santos 2006; Pek et al. 2008; Mandolesi and Jones 2012; Marti, 2014; Wang et al. 2017; Cao et al. 2018; Kong et al. 2018; Xiao et al. 2019; Luo et al. 2020) have focused on the influence from just the axial or the diagonal resistivity elements of (1). They found that ρ_x has a strong impact on the Z_{xy} , Z_{yy} and T_y responses, and a weaker impact on the other half. On the other hand, ρ_y strongly affects the Z_{yx} , Z_{xx} and T_x responses, and has a lesser effect on the other half. This strong influence is the reason why most of the earlier axial anisotropic inversions have shown a successful recovery of these ρ_x and ρ_y elements (e.g., Pek and Santos 2006; Marti, 2014; Cao et al. 2018; Luo et al. 2020; Kong et al. 2021; Rong et al. 2022).

In contrast to the ρ_x and ρ_y elements, the ρ_z element has a very weak influence on all MT responses as many different values of ρ_z have turned out to produce similar magnitudes of responses. This causes a big ambiguity and failure for the anisotropic inversion to recover the weak influence ρ_z element (e.g., Pek and Santos 2006; Wang et al. 2017; Cao et al. 2018; Luo et al. 2020; Kong et al. 2021; Rong et al. 2022). Cao et al. (2018) and Luo et al. (2020) explained that the weak influence of the ρ_z element is mostly due to the lack of the vertical electric field E_z at the surface according to the MT plane wave assumption.

Aside from the study of the influences of the principal axial resistivities, only Kong et al. (2018) have demonstrated the influence in the cases of the azimuthal anisotropy and the dipping anisotropy resulting from the rotational matrices, \mathbf{R}_z and \mathbf{R}_x , respectively. They found that the action of $\mathbf{R}_z(\alpha_S)$ has a high impact on all impedance components, while the action of $\mathbf{R}_x(\alpha_D)$ only affects the Z_{yx} and Z_{xx} responses. Continuing from their previous work Kong et al. (2018) and Kong et al. (2021), and recently, Rong et al. (2022) developed 3-D general anisotropic inversion to search for the three principal resistivities (ρ_x , ρ_y , and ρ_z), and the three anisotropy angles (α_S , α_D , and α_L). Although their 3-D general anisotropic inversion is better than the 3-D isotropic inversion, they also show that it is very challenging for the inversion to avoid the ambiguity of a mixture of anisotropy and heterogeneity of the models (Kong et al. 2021). Rong et al. (2022) also showed difficulty in recovering all anisotropy parameters of (2). Our goal of understanding the influence of all aspects of the anisotropy elements would be helpful in this case.

To study the influence of each resistivity element on the surface responses, we first introduce the influence index Z_{ij}^{inf} for each component of the impedance tensor, and the edge index T_i^{edge} for each component of the tipper, where i and j are the x - or y -directions. These influence indices will help to quantify the influence for each of the resistivity elements to avoid being subjective. Then we repeat the influence studies using our influence indices on the axial cases, as in Pek and Santos (2006), Marti (2014), Cao et al. (2018), Luo et al. (2020), Kong et al. (2021), and also through the rotational matrices as in Kong et al. (2018). We later apply the influence indices to study the effects of the off-diagonal resistivity elements in the cases of azimuthal anisotropy and dipping anisotropy. In the discussion and conclusion, we use all observations obtained from these studies to design two new processes for 3-D anisotropic inversion.

The 3-D anisotropic/isotropic synthetic models

Our 3-D anisotropic/isotropic model (Fig. 1) for this study is adapted from the 2-D model by Pek et al. (2008) (also shown in Fig. 14a in the Appendix). There are two isotropic layers (Fig. 1b): the top 300 Ω -m layer is 5 km thick and lies on top of an isotropic 1000 Ω -m half-space medium. In addition, there is a 3-D anisotropic/isotropic body with lengths of 50 km in both horizontal directions (Fig. 1a) and a thickness of 4 km (Fig. 1b). This 3-D anisotropic/isotropic body will be buried at the surface and at depths of 5 km, and 20 km.

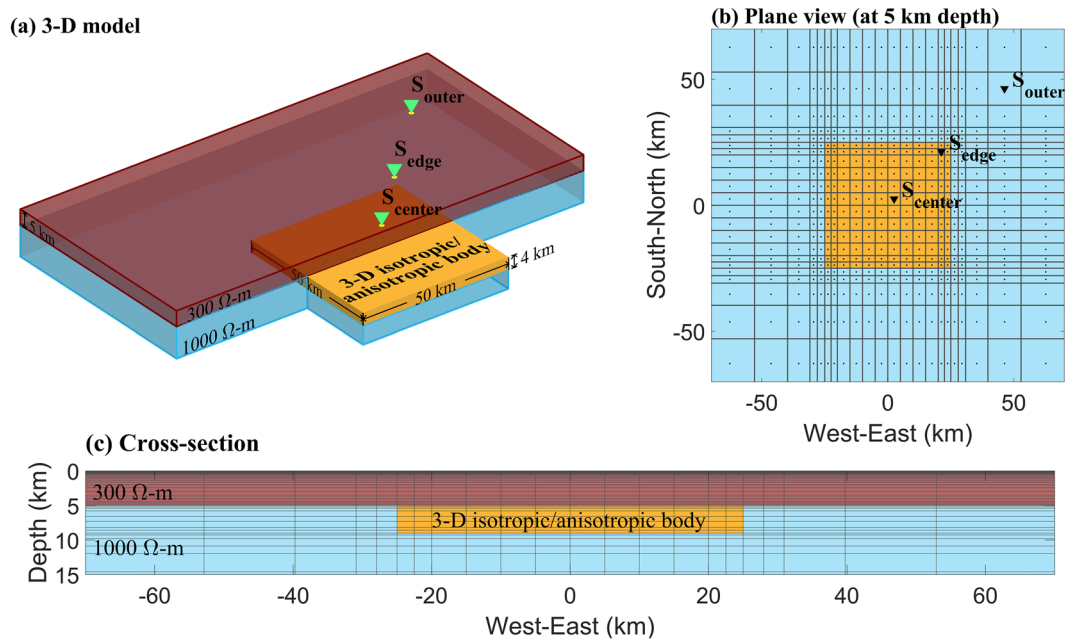


Fig. 1 **a** Three-dimensional isotropic/anisotropic model adapted from the 2-D model of Pek et al. (2008) for the case where the 3-D body is buried at a depth of 5 km. **b** Plane view at a depth of 5 km. **c** Cross-section along west–east direction (y -axis). The two isotropic 300 Ω -m and 1000 Ω -m layers are kept fixed. Only the 3-D body will be changed to either anisotropic or isotropic resistivity with various resistivity values. The 3-D body was buried at various depths: 0 km (surface), 5 km (shown above), and 20 km. Dots at the surface on **b** are the 484 MT stations used in this study. S_{center} , S_{edge} , and S_{outer} are the stations discussed in the next section

The 3-D model in Fig. 1 was discretized to $42 \times 42 \times 70$ in the x -, y - and vertical z -directions, respectively. Over the area of interest within a $120 \text{ km} \times 120 \text{ km}$ region (Fig. 1a), we have set up a total of 484 stations at the center of each cell on the surface. Three stations (S_{center} , S_{edge} , and S_{outer} in Fig. 1a) will be used to demonstrate our observations for the isotropic cases: S_{center} is close to the center of the 3-D anisotropic body, S_{edge} is just inside the edge of the 3-D body, and S_{outer} is the outer edge of the 3-D body (Fig. 1a).

For the isotropic 3-D body models, the resistivity of the 3-D body takes the values 0.5, 5, 50, 500, and 5000 Ω -m, and these models are referred to as the iso05, iso5, iso50, iso500, and iso5000 models, respectively. To get the responses for all 484 stations at the surface, we run the WSINV3DMT forward code (Siripunvaraporn and Egbert 2002, 2009; Siripunvaraporn et al. 2005) with periods from 0.001 to 1000 s (a total of 19 periods) covering the ranges used in most MT explorations. Among these isotropic models, iso50 is chosen as the reference isotropic model as its resistivity is the median of the cases we examined.

For the anisotropic studies, we varied the “assigned” anisotropic resistivity element of the 3-D body according to the set of resistivities used in the isotropic cases in the axial case (section “The axial anisotropy”), and

the conditions on the dipping and azimuthal cases (section “The R_x dipping anisotropy”, “The R_y dipping anisotropy” and “The azimuthal anisotropy”). The results from the anisotropic models will be compared with the reference iso50 model in the axial case (section “The axial anisotropy”) or any assigned references later in section “The R_x dipping anisotropy”, “The R_y dipping anisotropy”, and “The azimuthal anisotropy”. The anisotropic forward code used in our study is described in Appendix A. The anisotropic forward models were applied with the same sets of period ranges as for the isotropic studies.

The impedance tensor influence and tipper edge effect indices

The impedance tensor influence indices

To justify the strong and weak effects of the surface impedance tensor responses Z_{xy} , Z_{yx} , Z_{xx} , and Z_{yy} from the buried 3-D resistivity bodies, we introduce the impedance tensor influence index Z_{ij}^{inf} . The impedance tensor influence index for a given station s at the surface $Z_{ij}^{inf}(s)$ is defined as the root-mean-square (RMS) difference between a given impedance response $Z_{ij}(s)$, and the reference impedance response $Z_{ij}^{ref}(s)$ normalized with the average of the products of the off-diagonal impedances between the given model and the reference model, i.e.,

$$Z_{ij}^{\text{inf}}(s) = \sqrt{\frac{1}{N_p} \sum_p \frac{|Z_{ij}(p, s) - Z_{ij}^{\text{ref}}(p, s)|^2}{(|Z_{xy}(p, s)Z_{yx}(p, s)| + |Z_{xy}^{\text{ref}}(p, s)Z_{yx}^{\text{ref}}(p, s)|)/2}}, \quad (3)$$

where p is the period, N_p is the number of periods, and i and j are either x or y . The overall impedance tensor influence index Z_{ij}^{inf} for all stations is defined similarly as

$$Z_{ij}^{\text{inf}} = \sqrt{\frac{1}{N_s} \frac{1}{N_p} \sum_s \sum_p \frac{|Z_{ij}(p, s) - Z_{ij}^{\text{ref}}(p, s)|^2}{(|Z_{xy}(p, s)Z_{yx}(p, s)| + |Z_{xy}^{\text{ref}}(p, s)Z_{yx}^{\text{ref}}(p, s)|)/2}}, \quad (4)$$

where s is the station, and N_s is the number of stations.

To demonstrate the functionalities of these four indices, Z_{xx}^{inf} , Z_{xy}^{inf} , Z_{yx}^{inf} and Z_{yy}^{inf} , for Z_{xx} , Z_{xy} , Z_{yx} and Z_{yy} , respectively, we first applied them to the isotropic cases (iso05, iso5, iso500, iso5000) at all stations in Fig. 1 with the 3-D body at various depths. We used the iso50 models of their corresponding 3-D bodies as the references. For each type of responses, the overall Z_{ij}^{inf} indices for each of the isotropic cases are shown in the top row of Fig. 2a, while those at the center, edge, and outer stations (S_{center} , S_{edge} and S_{outer} , respectively) are shown in the bottom row of Fig. 2a.

The overall Z_{xy}^{inf} and Z_{yx}^{inf} indices of all cases are higher than those of the overall Z_{xx}^{inf} and Z_{yy}^{inf} indices (Fig. 2a).

All of our influence indices, Z_{xx}^{inf} , Z_{xy}^{inf} , Z_{yx}^{inf} and Z_{yy}^{inf} also show that they are a function of depth of the buried 3-D body. The strongest influence occurs when the 3-D body is at the surface and decreases when the 3-D body is deeper. For the station impedance tensor indices, $Z_{ij}^{\text{inf}}(s)$ at the center S_{center} and at the inner edge S_{edge} clearly show that the 3-D resistivity body has more influence on

the Z_{xy} and Z_{yx} responses than those at the outer station S_{outer} . For Z_{xx} and Z_{yy} , the station influences are strong only around the edges and corners of the 3-D body, e.g., at the S_{edge} station (Fig. 2a). Far away from the edge, the influence has gradually diminished, e.g., at the S_{outer} and S_{center} stations. This is also revealed in the surface plots of the influence impedance tensor indices $Z_{xx}^{\text{inf}}(s)$, $Z_{xy}^{\text{inf}}(s)$, $Z_{yx}^{\text{inf}}(s)$ and $Z_{yy}^{\text{inf}}(s)$ from the iso5 and iso500 models where the 3-D body is 5 km deep in Fig. 3a and b, respectively.

We then performed the 3-D isotropic inversion (Siripunvaraporn and Egbert 2009; Siripunvaraporn et al. 2005) on the three isotropic data sets (the 3-D body was buried at the surface, at 5 km, and at 20 km) with 2% Gaussian noise and with the two-layer model in Fig. 1 as the initial model.

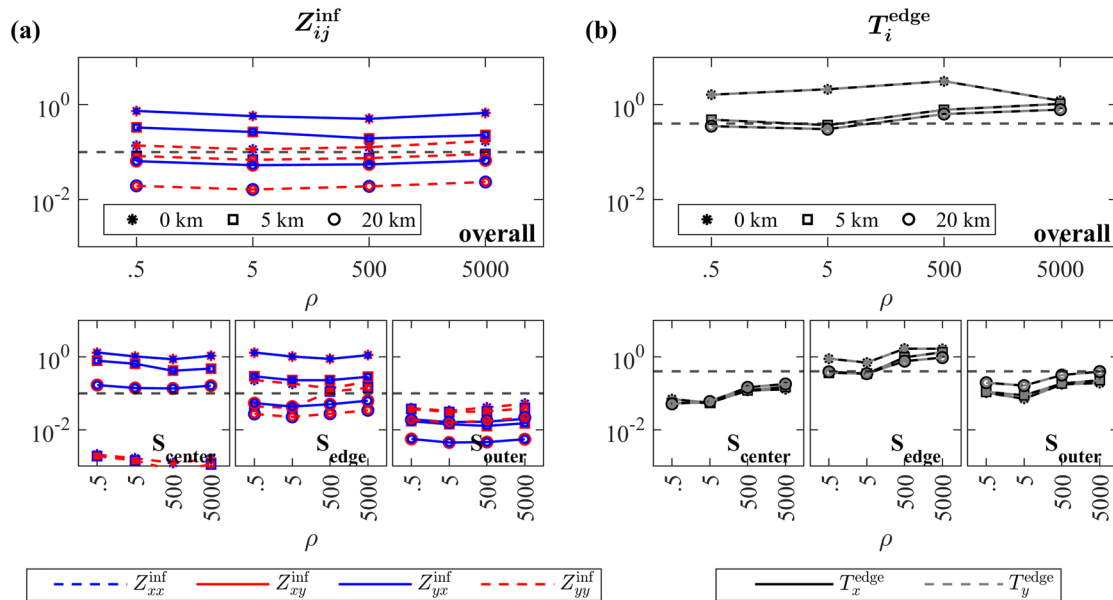


Fig. 2 **a** The impedance tensor influence indices Z_{xx}^{inf} , Z_{xy}^{inf} , Z_{yx}^{inf} and Z_{yy}^{inf} , and **b** the tipper edge effect indices T_x^{edge} and T_y^{edge} calculated with all stations according to (4) and (6), respectively, and just at the S_{center} , S_{edge} , and S_{outer} stations, Eqs. (3) and (51), for the isotropic experiments where the resistivity of the 3-D body is varied as shown on the x-axis and buried at the surface, 5 km and 20 km. The dashed lines are at 0.1 for the impedance tensor and 0.50 for the tipper and mark the 10% and 50% levels, respectively

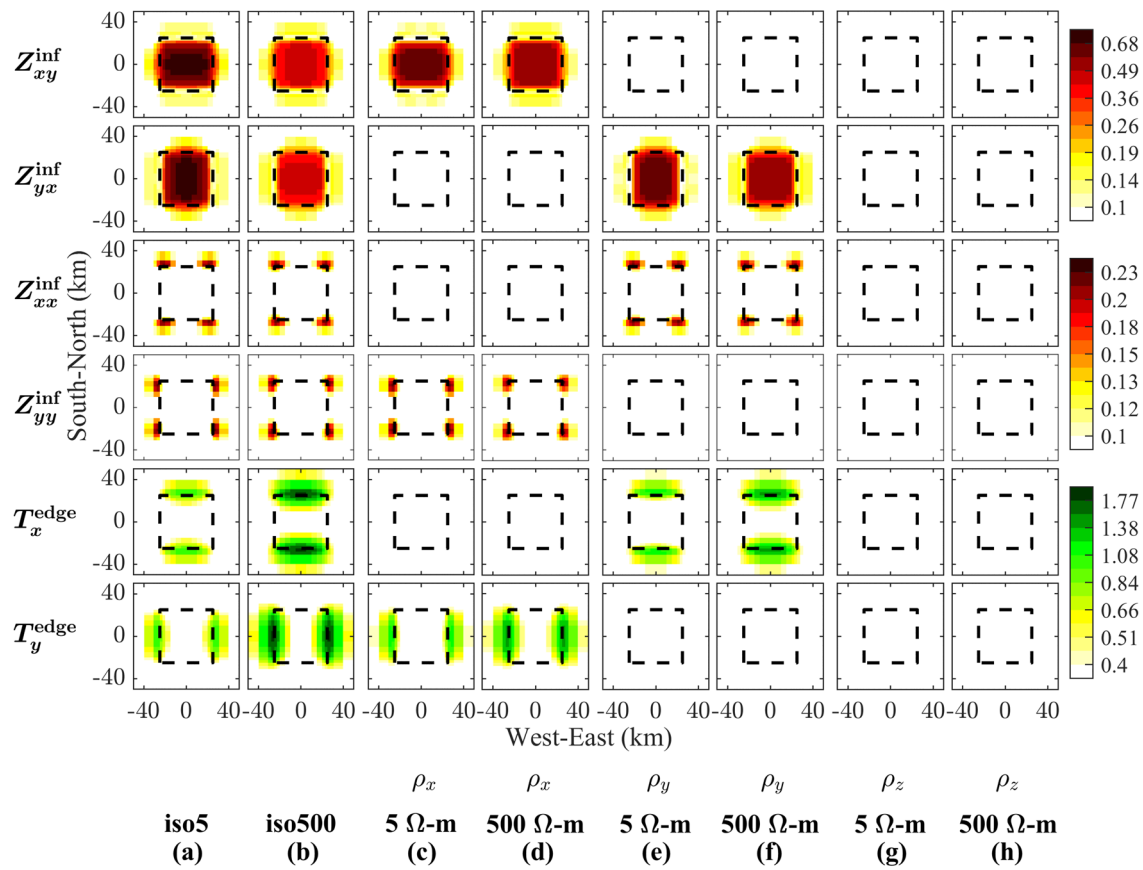


Fig. 3 The surface logarithmic plot of the impedance tensor influence indices $Z_{xy}^{\text{inf}}(s)$, $Z_{yx}^{\text{inf}}(s)$, $Z_{xx}^{\text{inf}}(s)$, and $Z_{yy}^{\text{inf}}(s)$ and the tipper edge effect indices $T_x^{\text{edge}}(s)$, and $T_y^{\text{edge}}(s)$ at all 484 stations from top to bottom rows, respectively, obtained from (a) the iso5 model, (b) the iso500 model (c) $\rho_x = 5 \Omega\text{-m}$, (d) $\rho_x = 500 \Omega\text{-m}$, (e) $\rho_y = 5 \Omega\text{-m}$, (f) $\rho_y = 500 \Omega\text{-m}$, (g) $\rho_z = 5 \Omega\text{-m}$, and (h) $\rho_z = 500 \Omega\text{-m}$, respectively, where the buried depth of the 3-D body in Fig. 1 (shown as dashed square) is 5 km

We found that the stronger influence bodies (the 3-D body was buried at the surface, and at 5 km) can be recovered but the weaker influence body at a depth of 20 km cannot. The overall influence level defined in (4) and the inversion RMS misfit (e.g., Siripunvaraporn and Egbert 2000, 2009; Siripunvaraporn et al. 2005; Siripunvaraporn and Sarakorn 2011; Siripunvaraporn 2012; Cao et al. 2018; Luo et al. 2020; Kong et al. 2021) are defined similarly so both can be linked. When the influence level is high for a wide range of resistivity values of the 3-D body, the inversion can also generate different inversion RMS misfits from the same resistivity range. Thus, there would be no difficulties for the 3-D isotropic inversion to recover the 3-D isotropic resistivity structure, even with just the Z_{xy} and Z_{yx} responses. However, when the 3-D body is buried at a greater depth (e.g., at 20 km), the influence of all components drops (below the 10% level for Z_{xy} , Z_{yx} , Z_{xx} and Z_{yy} in Fig. 2) even with different resistivity values. This makes it difficult for the inversion to distinguish these different resistivities resulting in similar RMS misfits. It is therefore

not possible for the 3-D isotropic inversion to recover these weak influence structures.

Using this recovery criterion, the 10% influence level for Z_{xy}^{inf} and Z_{yx}^{inf} in Fig. 2a appears to be a good indicator to distinguish between the strong and weak influence for the isotropic cases. We will then keep this level as the minimum level for the anisotropic tests in the next sections. Since Z_{xx} and Z_{yy} cannot be inverted without Z_{xy} and Z_{yx} , this is consistent with Z_{xx}^{inf} and Z_{yy}^{inf} showing a relatively low influence (Fig. 2a), mostly below the 10% level. The strong and weak influence of Z_{xx}^{inf} and Z_{yy}^{inf} is therefore based on their comparative values. However, we still prefer to use the 10% separation level of Z_{xy}^{inf} and Z_{yx}^{inf} as a reference for Z_{xx}^{inf} and Z_{yy}^{inf} .

The tipper edge effect indices

Since the tippers T_x and T_y are very sensitive to the lateral resistivity change or the edge of structures, like Z_{xx} and Z_{yy} , this value is high only near the edge of the structure

and vanishes away from the edge (Siripunvaraporn and Egbert 2009). Applying (3) and (4) directly for the tipper would cause large errors for stations in the center or far away from the edge as their values at these stations are low. Thus, for the tipper, the influence is re-defined as the tipper edge effect indices T_i^{edge} with the purpose of measuring the influence from the edge of the 3-D structures. To do that, we need to fix the tipper of the inner edge station S_{edge} of the reference case as a normalized term for all stations. For each station s , the tipper edge effect $T_i^{\text{edge}}(s)$ is then

$$T_i^{\text{edge}}(s) = \sqrt{\frac{1}{N_p} \sum_p \frac{|T_i(p, s) - T_i^{\text{ref}}(p, s)|^2}{[|T_x^2(p, e)| + |T_y^2(p, e)| + |T_x^{2, \text{ref}}(p, e)| + |T_y^{2, \text{ref}}(p, e)|]/4}}, \quad (5)$$

where e is the station at the edge or S_{edge} , and i is either x or y . The overall tipper edge effect index T_i^{edge} for all stations is defined as

$$T_i^{\text{edge}} = \sqrt{\frac{1}{N_s} \frac{1}{N_p} \sum_s \sum_p \frac{|T_i(p, s) - T_i^{\text{ref}}(p, s)|^2}{[|T_x^2(p, e)| + |T_y^2(p, e)| + |T_x^{2, \text{ref}}(p, e)| + |T_y^{2, \text{ref}}(p, e)|]/4}}. \quad (6)$$

In addition to (5) and (6), the cutoff amplitude of the tipper in our study cases is set at 0.004 to avoid the instability of the indices. For the isotropic cases, the overall tipper edge effect indices T_x^{edge} and T_y^{edge} from all stations, and $T_x^{\text{edge}}(s)$ and $T_y^{\text{edge}}(s)$ at S_{center} , S_{edge} and S_{outer} are shown in Fig. 2b.

For all stations, the overall T_x^{edge} and T_y^{edge} indices are generally high (Fig. 2b) and roughly the same even from different resistivity objects at different depths. The strong edge effect levels are mostly from the stations around the edge as demonstrated at the S_{edge} station, while far from the edges, there is a weak effect at the S_{center} and S_{outer} stations. This can be clearly seen from the surface plots of the edge effect indices T_x^{edge} and T_y^{edge} from the iso5 and iso500 models in Fig. 3a and b, respectively, where the depth of the 3-D body is 5 km.

As with the impedance tensor cases, here we inverted just the tipper data of each case with the two-layer model (Fig. 1) as an initial model with the isotropic inversion code. Most of the inverted models put the lateral resistivity change of the 3-D anomaly at the surface, not at their corresponding depths, as is also demonstrated in Fig. 6 of Siripunvaraporn and Egbert (2009). Thus, the only case when the tipper data alone can recover the anomaly is when the 3-D body is at or close to the surface.

As for Z_{xx} and Z_{yy} , the T_x and T_y data need Z_{xy} and Z_{yx} to correctly recover the anomaly. Thus, the strong and weak influence of T_x^{edge} and T_y^{edge} is just based on their comparative values, as with those of Z_{xx}^{inf} and Z_{yy}^{inf} . However, all T_x^{edge} and T_y^{edge} at the S_{edge} station are well above the 50% level, while they are lower at S_{outer} and S_{center} . We therefore use this 50% level as a reference for our anisotropic studies in the next sections. Note here that the 10% level for the impedance tensor and 50% level for the tipper are only applicable for our tests and can be different for other tests.

The influence of various types of the anisotropy

In this section, we give the results of many experiments to learn about the influence of the anisotropic resistivity elements on the surface responses via many different types of anisotropic 3-D bodies. We prefer to report the facts observed from the experiments in this section. We will then discuss and summarize these observations in the next section.

The axial anisotropy

In our first experiment, the goal is to measure the influence and the edge effect using our Z_{ij}^{inf} and T_i^{edge} indices, respectively, in the case when the 3-D resistivity body of

Fig. 1 has axial anisotropy, i.e., $\hat{\rho} = \begin{bmatrix} \rho_x & 0 & 0 \\ 0 & \rho_y & 0 \\ 0 & 0 & \rho_z \end{bmatrix}$, relative

to the 3-D isotropic body of the iso50 case. To see the influence of the ρ_x element, we kept $\rho_y = \rho_z = 50 \Omega\text{-m}$ and varied ρ_x of the 3-D body ($\rho_x = 0.5, 5, 500$, and $5000 \Omega\text{-m}$) for each of the depths (0, 5 and 20 km). Since the 20 km depth case yields very low indices for all cases, as in the isotropic cases, it will not be included in any figures after this section. Similarly, to see the influence of the ρ_y or ρ_z elements, we kept other elements constant at

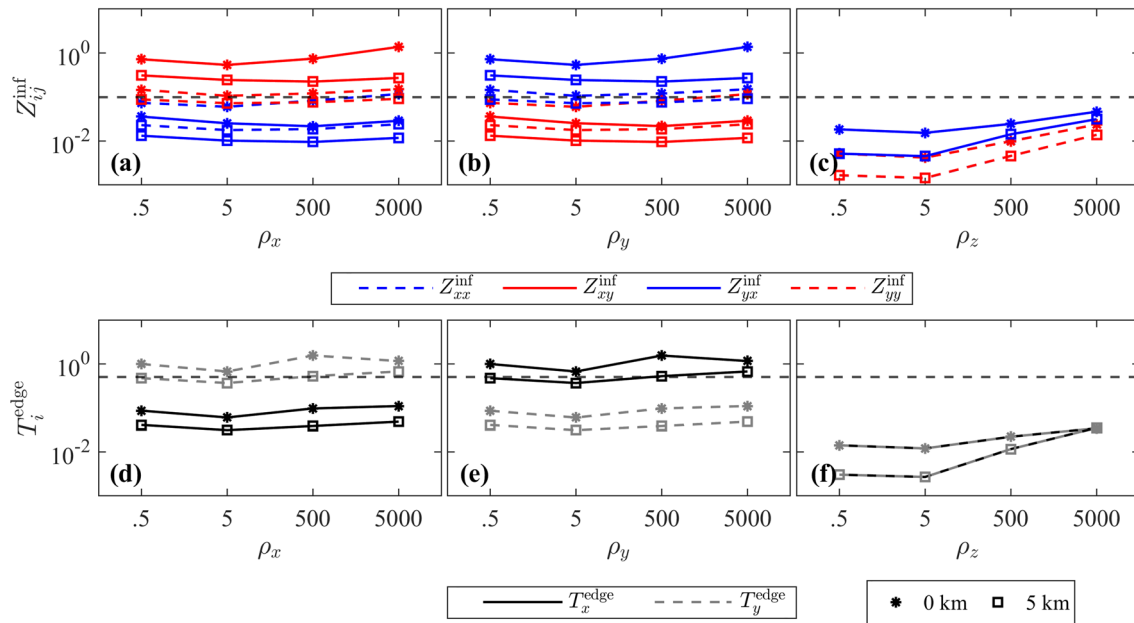


Fig. 4 (top) Logarithmic plots of the overall impedance tensor influence index Z_{xx}^{inf} , Z_{yy}^{inf} , Z_{xy}^{inf} , and Z_{yx}^{inf} when varying **a** ρ_x , **b** ρ_y , and **c** ρ_z , respectively. (bottom) Logarithmic plots of the overall tipper edge effect indices T_x^{edge} and T_y^{edge} when varying **d** ρ_x , **e** ρ_y , and **f** ρ_z , respectively. The varying resistivity values are shown on the x-axis. The dashed lines mark 10% for Z_{ij}^{inf} and 50% for T_i^{edge} for reference. The asterisk and square are for the cases where the buried depth of the 3-D body is 0 km and 5 km, respectively

50 Ω -m, and then varied ρ_y or ρ_z with the same sets of resistivities used in the ρ_x cases.

Each case was simulated separately with our 3-D anisotropic forward code (see Appendix A) to obtain the \mathbf{Z} and \mathbf{T} responses at all 484 stations with 19 periods. The overall and station Z_{ij}^{inf} and T_i^{edge} indices were then applied to the responses obtained from all cases. Examples of the apparent resistivities and the magnitude of the tipper at a period of 10 s for the case where the 3-D body is at 5 km deep are shown in Fig. 15 of Appendix A.

Figure 3 shows the surface plots of the station Z_{ij}^{inf} (s) and T_i^{edge} (s) indices for every station of Fig. 1, when ρ_x (Fig. 3c and d), ρ_y (Fig. 3e and f), and ρ_z (Fig. 3g and h) are 5 and 500 Ω -m. We also plot the isotropic cases iso5 (Fig. 3a) and iso500 (Fig. 3b), respectively, for the case where the 3-D body is 5 km deep. Similar influence and edge effect patterns with different magnitudes can also be obtained from other buried depths of the 3-D body. In Fig. 3, we use white to indicate when the influence and edge effects are very weak (below 10% and 50%, respectively). For the isotropic cases (Fig. 3a and b), the impacts of the 3-D body buried at 5 km depth on all responses are obvious. They are larger for the stations above the 3-D body for Z_{xy} and Z_{yx} , and around the edges and corners for Z_{xx} , Z_{yy} , T_x and T_y .

In the case of the axial anisotropy, ρ_x shows strong influence on Z_{xy} mostly above the 3-D anisotropic body, and around the edges and corners on Z_{yy} and T_y . It has a weak influence on Z_{yx} , Z_{xx} , and T_x (Fig. 3c and d). The same influences and edge effects as in Fig. 3c and d can also be observed when the 3-D body is buried at other depths. The strong impacts on Z_{xy} , Z_{yy} and T_y from ρ_x is confirmed with the overall Z_{ij}^{inf} and T_i^{edge} indices shown in Fig. 4a and d for the cases where the buried depth of the 3-D body is 0 and 5 km. Figure 4a and d also shows that ρ_x has a very weak impact on the Z_{yx} , Z_{xx} , and T_x responses.

For the ρ_y cases (Fig. 3e and f), the effects are the opposite of the ρ_x cases. The ρ_y element strongly affects the Z_{yx} , Z_{xx} , and T_x responses, and has a weak influence on Z_{xy} , Z_{yy} , and T_y . This agrees with the overall influence and edge effect indices shown in Fig. 4b and e. Interestingly, Fig. 3g and h for ρ_z shows mostly white patterns in agreement with the very low overall influence and edge effect indices in Fig. 4c and f. This indicates that ρ_z has a very weak influence on all responses. This is confirmed in Fig. 15 where the response of the ρ_z cases is almost identical to those from the iso50 model, regardless of the resistivity values.

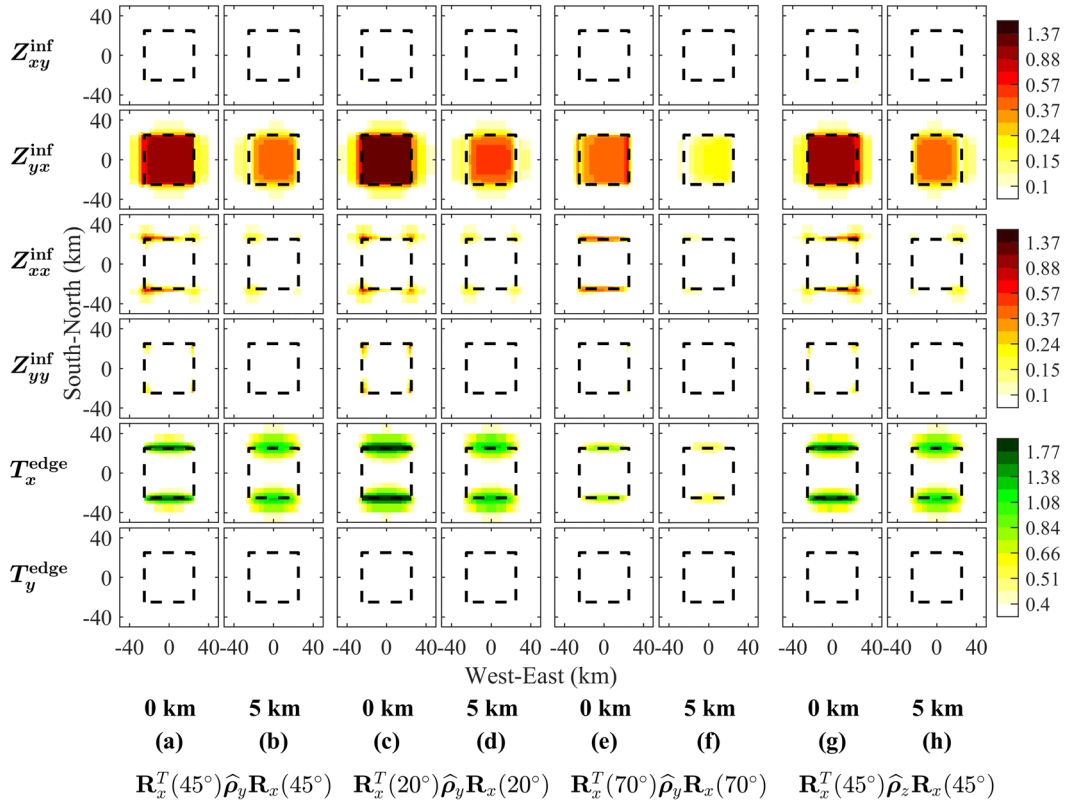


Fig. 5 The surface logarithmic plot of $Z_{xy}^{\text{inf}}(s)$, $Z_{yx}^{\text{inf}}(s)$, $Z_{xx}^{\text{inf}}(s)$, and $Z_{yy}^{\text{inf}}(s)$, and $T_x^{\text{edge}}(s)$, and $T_y^{\text{edge}}(s)$ at all 484 stations from top to bottom rows, respectively, obtained when the 3-D anisotropic body in Fig. 1 (shown as dashed line) is assigned with $\mathbf{R}_x^T(45^\circ)\hat{\rho}_y\mathbf{R}_x(45^\circ)$ and buried at **a** the surface (0 km), and **b** 5 km deep, given $\hat{\rho}_y = \begin{bmatrix} 50 & 0 & 0 \\ 0 & 500 & 0 \\ 0 & 0 & 50 \end{bmatrix}$, and similarly with $\mathbf{R}_x^T(20^\circ)\hat{\rho}_y\mathbf{R}_x(20^\circ)$ for **c** and **d**, and with $\mathbf{R}_x^T(70^\circ)\hat{\rho}_y\mathbf{R}_x(70^\circ)$ for **e** and **f**. In addition, when the 3-D anisotropic body is assigned with $\mathbf{R}_x^T(45^\circ)\hat{\rho}_z\mathbf{R}_x(45^\circ)$, given $\hat{\rho}_z = \begin{bmatrix} 50 & 0 & 0 \\ 0 & 50 & 0 \\ 0 & 0 & 500 \end{bmatrix}$, the results are also shown in g and h

In summary, for the axial anisotropy, ρ_x strongly affects Z_{xy} , Z_{yy} , and T_y , whereas ρ_y has strong effects on Z_{yx} , Z_{xx} , and T_x . In contrast, ρ_z does not affect any responses. Our influence studies with our Z_{ij}^{inf} and T_i^{edge} indices are in agreement with most previous studies (Pek and Santos 2006; Wang et al. 2017; Cao et al. 2018; Luo et al. 2020; Kong et al. 2021).

The \mathbf{R}_x dipping anisotropy

When applying the rotation matrix around the x -axis, \mathbf{R}_x , to both sides of the axial resistivity tensor $\hat{\rho}$, we obtain the dipping anisotropy, i.e., $\mathbf{R}_x^T(\theta)\hat{\rho}\mathbf{R}_x(\theta) = \begin{bmatrix} \rho_{xx} & 0 & 0 \\ 0 & \rho_{yy} & \rho_{yz} \\ 0 & \rho_{zy} & \rho_{zz} \end{bmatrix}$. The influence on the surface responses from the rotation matrix \mathbf{R}_x is therefore equivalent to the influence from a combination of ρ_{xx} , ρ_{yy} , ρ_{zz} and $\rho_{yz} - \rho_{zy}$. In this section, we first

investigate the influence of this rotation matrix \mathbf{R}_x on the surface responses, and then we explore the influence and the role of ρ_{xx} , ρ_{yy} , ρ_{zz} and $\rho_{yz} - \rho_{zy}$, one by one.

The effect of \mathbf{R}_x

To see the influence from the rotation matrix \mathbf{R}_x or the combination ρ_{xx} , ρ_{yy} , ρ_{zz} and $\rho_{yz} - \rho_{zy}$ on the surface responses, we first performed $\mathbf{R}_x^T(\theta)\hat{\rho}_y\mathbf{R}_x(\theta)$ with various θ on the 3-D anisotropic body (Fig. 1) with $\hat{\rho}_y = \begin{bmatrix} 50 & 0 & 0 \\ 0 & 500 & 0 \\ 0 & 0 & 50 \end{bmatrix}$ ($\Omega\cdot\text{m}$). Figure 5a and b shows the station influence and edge effect of the responses, $Z_{xy}^{\text{inf}}(s)$, $Z_{yx}^{\text{inf}}(s)$, $Z_{xx}^{\text{inf}}(s)$, $Z_{yy}^{\text{inf}}(s)$, $T_x^{\text{edge}}(s)$, and $T_y^{\text{edge}}(s)$ from the action of $\mathbf{R}_x^T(45^\circ)\hat{\rho}_y\mathbf{R}_x(45^\circ)$ for the case where the 3-D anisotropic body is at depth of 0 and 5 km, respectively, and similarly for Fig. 5c and d for $\mathbf{R}_x^T(20^\circ)\hat{\rho}_y\mathbf{R}_x(20^\circ)$, and

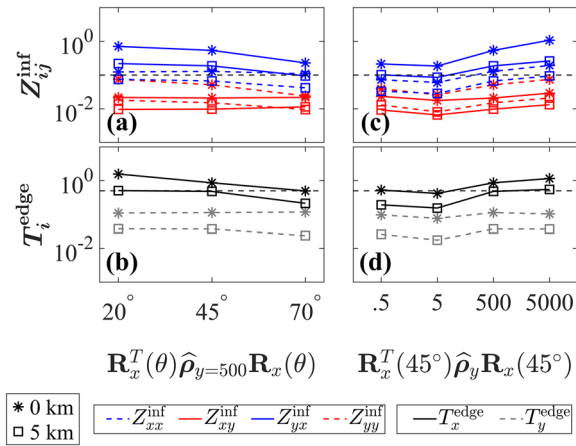


Fig. 6 **a** Logarithmic plots of Z_{xx}^{inf} , Z_{yy}^{inf} , Z_{xy}^{inf} , and Z_{yx}^{inf} and **b** T_x^{edge} , and T_y^{edge} with $\mathbf{R}_x^T(\theta)\hat{\rho}_y\mathbf{R}_x(\theta)$, and $\hat{\rho}_y = \begin{bmatrix} 50 & 0 & 0 \\ 0 & 500 & 0 \\ 0 & 0 & 50 \end{bmatrix}$, when $\theta = 20^\circ, 45^\circ, 70^\circ$ shown on x-axis. Similarly, **c** and **d** are for $\mathbf{R}_x^T(45^\circ)\hat{\rho}_y\mathbf{R}_x(45^\circ)$, when $\hat{\rho}_y = \begin{bmatrix} 50 & 0 & 0 \\ 0 & \rho_y & 0 \\ 0 & 0 & 50 \end{bmatrix}$ with ρ_y equaling 0.5, 5, 500, and 5000 $\Omega\text{-m}$ shown on the x-axis

Fig. 5e and f for $\mathbf{R}_x^T(70^\circ)\hat{\rho}_y\mathbf{R}_x(70^\circ)$. In addition, performing $\mathbf{R}_x^T(45^\circ)\hat{\rho}_z\mathbf{R}_x(45^\circ)$, when $\hat{\rho}_z = \begin{bmatrix} 50 & 0 & 0 \\ 0 & 50 & 0 \\ 0 & 0 & 500 \end{bmatrix}$ ($\Omega\text{-m}$) (Fig. 5g and h) yields symmetrical images about the x-axis of Fig. 5a and b for the impedance tensor indices but not the tippers (due to a fixed edge station as reference).

It is clear from Fig. 5a–f that \mathbf{R}_x , regardless of θ , has a strong impact on Z_{yx} for the stations above the 3-D body, and on the Z_{xx} and T_x responses for the stations around the edges and corners. The action of $\mathbf{R}_x^T(\theta)\hat{\rho}_y\mathbf{R}_x(\theta)$ when $\theta = 20^\circ$ (Fig. 5c and d) yields a higher influence than those of other angles (Fig. 5a, b, e and f). The influence is reversed for $\mathbf{R}_x^T(\theta)\hat{\rho}_z\mathbf{R}_x(\theta)$ which has higher influence when $\theta = 70^\circ$. Both facts are confirmed by the overall Z_{xx}^{inf} , Z_{yy}^{inf} , Z_{xy}^{inf} , Z_{yx}^{inf} , T_x^{edge} , and T_y^{edge} indices in Fig. 6a and b demonstrating stronger influence on the Z_{yx} , Z_{xx} and T_x responses. The level of the influence decreases when the 3-D body is buried deeper.

In the next experiment, we performed $\mathbf{R}_x^T(45^\circ)\hat{\rho}_y\mathbf{R}_x(45^\circ)$ on the 3-D anisotropic body (Fig. 1) with ρ_y at 0.5, 5, 500 and 5000 $\Omega\text{-m}$ when $\hat{\rho}_y = \begin{bmatrix} 50 & 0 & 0 \\ 0 & \rho_y & 0 \\ 0 & 0 & 50 \end{bmatrix}$ ($\Omega\text{-m}$). The results with different ρ_y yield similar patterns to those in Fig. 5a–f with different amplitude levels. The influence indices from these cases are shown in Fig. 6c and d. As with the case with

various angles, the stronger influences are seen on the Z_{yx} , Z_{xx} and T_x responses and there is a very weak influence on the Z_{xy} , Z_{yy} and T_y responses. Surprisingly, the higher ρ_y appear to have a higher influence than the lower resistivities.

The strong and weak influences from the action of \mathbf{R}_x (Fig. 6a–d), regardless of the θ and resistivity values, are apparently equivalent to the action from the ρ_y element of the axial cases demonstrated in section "The axial anisotropy" (Fig. 4b and e). However, in this case, the action of \mathbf{R}_x is in fact a contribution from the combination of ρ_{xx} , ρ_{yy} , ρ_{zz} and $\rho_{yz} - \rho_{zy}$.

The effect of each of ρ_{xx} , ρ_{yy} , ρ_{zz} and $\rho_{yz} - \rho_{zy}$ on the surface responses

To investigate the roles and contributions from each of ρ_{xx} , ρ_{yy} , ρ_{zz} and $\rho_{yz} - \rho_{zy}$ on the surface response, we vary one element at a time while keeping other elements constant. The variation of ρ_{yy} , ρ_{zz} , and ρ_{yz} carried out while satisfying the condition $\rho_{zz}\rho_{yy} > \rho_{yz}^2$, in order to guarantee that this given structure can be reversed to yield reasonable axial resistivity tensor and dipping angle (see Appendix B for more details).

In our case, given $\hat{\rho}_y = \begin{bmatrix} 50 & 0 & 0 \\ 0 & 500 & 0 \\ 0 & 0 & 50 \end{bmatrix}$, then

$$\mathbf{R}_x^T(45^\circ)\hat{\rho}_y\mathbf{R}_x(45^\circ) = \begin{bmatrix} 50 & 0 & 0 \\ 0 & 275 & 225 \\ 0 & 225 & 275 \end{bmatrix} \text{ which has all the}$$

terms ρ_{xx} , ρ_{yy} , ρ_{zz} and $\rho_{yz} - \rho_{zy}$ from \mathbf{R}_x . To see the effect of ρ_{yy} after the \mathbf{R}_x rotation on the surface response, the

tensor that we need to consider now is $\begin{bmatrix} 50 & 0 & 0 \\ 0 & \rho_{yy} & 225 \\ 0 & 225 & 275 \end{bmatrix}$, in

which ρ_{yy} must be in the range $(184, \infty)$ $\Omega\text{-m}$, according to the condition above. Here, ρ_{yy} is set to 2000 and 5000 $\Omega\text{-m}$. We still use the same indices Z_{xx}^{inf} , Z_{yy}^{inf} , Z_{xy}^{inf} , Z_{yx}^{inf} , T_x^{edge} , and T_y^{edge} to measure the influence of the variation on the surface response. However, in this case, the reference is directly with respect to

$$\mathbf{R}_x^T(45^\circ)\hat{\rho}_y\mathbf{R}_x(45^\circ) = \begin{bmatrix} 50 & 0 & 0 \\ 0 & 275 & 225 \\ 0 & 225 & 275 \end{bmatrix}, \text{ not the iso50}$$

model as in Fig. 6. The influence of ρ_{yy} in this case is shown in Fig. 7b.

Similar experiments were conducted for $\begin{bmatrix} \rho_{xx} & 0 & 0 \\ 0 & 275 & 225 \\ 0 & 225 & 275 \end{bmatrix}$, $\begin{bmatrix} 50 & 0 & 0 \\ 0 & 275 & \rho_{yz} \\ 0 & \rho_{yz} & 275 \end{bmatrix}$ and also $\begin{bmatrix} 50 & 0 & 0 \\ 0 & 275 & 225 \\ 0 & 225 & \rho_{zz} \end{bmatrix}$. According to the above condition (also see Appendix B), ρ_{zz} can be varied in the range $(184, \infty)$ $\Omega\text{-m}$ like ρ_{yy} ,

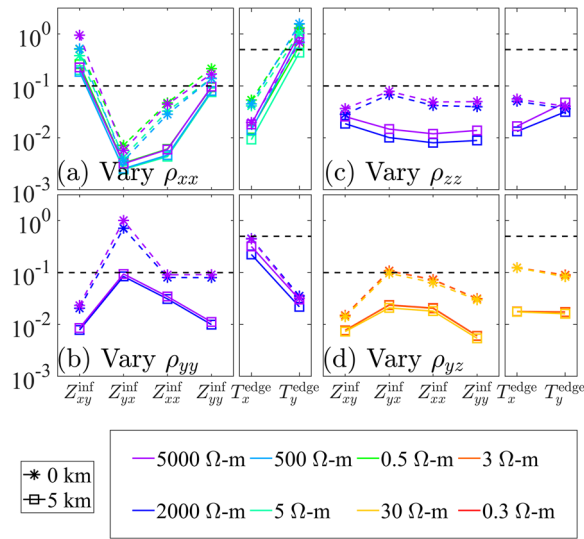


Fig. 7 The logarithmic plots of Z_{xy}^{inf} , Z_{yx}^{inf} , Z_{xx}^{inf} , Z_{yx}^{inf} , and T_x^{edge} on the x -axis for the case of $\mathbf{R}_x^T(45^\circ)\hat{\rho}_y\mathbf{R}_x(45^\circ)$ equaling **a**

$$\begin{bmatrix} \rho_{xx} & 0 & 0 \\ 0 & 275 & 225 \\ 0 & 225 & 275 \end{bmatrix} \text{ with } \rho_{xx} = 5000, 500, 5 \text{ and } 0.5 \text{ } \Omega\text{-m, } \mathbf{b}$$

$$\begin{bmatrix} 50 & 0 & 0 \\ 0 & \rho_{yy} & 225 \\ 0 & 225 & 275 \end{bmatrix} \text{ with } \rho_{yy} = 5000 \text{ and } 2000 \text{ } \Omega\text{-m, } \mathbf{c}$$

$$\begin{bmatrix} 50 & 0 & 0 \\ 0 & 275 & \rho_{yz} \\ 0 & \rho_{yz} & 275 \end{bmatrix} \text{ with } \rho_{yz} = 30, 3 \text{ and } 0.3 \text{ } \Omega\text{-m, and } \mathbf{d}$$

The indices are all with reference to $\mathbf{R}_x^T(45^\circ)\hat{\rho}_y\mathbf{R}_x(45^\circ)$, when $\hat{\rho}_y = \begin{bmatrix} 50 & 0 & 0 \\ 0 & 500 & 0 \\ 0 & 0 & 50 \end{bmatrix}$

while ρ_{yz} can be varied within the range (0, 275) Ω -m, and ρ_{xx} can have any value. Figure 7a shows the cases when ρ_{xx} is 0.5, 5, 500, and 5000 Ω -m when ρ_{yy} , ρ_{zz} and ρ_{yz} are kept fixed at 275, 275 and 225 Ω -m, respectively. When varying ρ_{zz} (Fig. 7c), we set ρ_{zz} to 2000 and 5000 Ω -m while the others are fixed. For the case of ρ_{yz} (Fig. 7d), it was set at 0.3, 3 and 30 Ω -m, while the other elements are fixed as well. The reference for all of Fig. 7 is with respect to $\mathbf{R}_x^T(45^\circ)\hat{\rho}_y\mathbf{R}_x(45^\circ)$.

Figures 5 and 6 show that \mathbf{R}_x or a combination of ρ_{xx} , ρ_{yy} , ρ_{zz} and $\rho_{yz} - \rho_{zy}$ has a strong influence on the Z_{yx} , Z_{xx} and T_x responses. Varying ρ_{xx} (Fig. 7a) while keeping the other elements fixed, surprisingly, does not affect any of the Z_{yx} , Z_{xx} and T_x responses, but does affect the Z_{xy} , Z_{yy} and T_y responses. Varying ρ_{yy} (Fig. 7b) while keeping the others fixed, we see a stronger influence on the Z_{yx} , Z_{xx} and T_x responses as with the original \mathbf{R}_x . Unexpected results are found on varying ρ_{zz} (Fig. 7c) or ρ_{yz} (Fig. 7d) as the influence indices Z_{xx}^{inf} , Z_{yy}^{inf} , Z_{xy}^{inf} , and Z_{yx}^{inf} are relatively low, and all below the reference levels. This

indicates that ρ_{zz} and ρ_{yz} turn out to contribute less to the strong influence responses Z_{yx} , Z_{xx} and T_x from \mathbf{R}_x (Figs. 5 and 6) than ρ_{yy} . Since ρ_{zz} and ρ_{yz} contribute less, it is possible to omit them. This will be discussed in the next section.

The \mathbf{R}_y dipping anisotropy

In section "The \mathbf{R}_x dipping anisotropy", we obtain the dipping anisotropy around the x -axis by performing

$$\mathbf{R}_x^T(\theta)\hat{\rho}\mathbf{R}_x(\theta) = \begin{bmatrix} \rho_{xx} & 0 & 0 \\ 0 & \rho_{yy} & \rho_{yz} \\ 0 & \rho_{zy} & \rho_{zz} \end{bmatrix}. \text{ Here, applying}$$

$$\mathbf{R}_y(\theta) = \begin{bmatrix} \cos\theta & 0 & \sin\theta \\ 0 & 1 & 0 \\ -\sin\theta & 0 & \cos\theta \end{bmatrix} \text{ on the axial resistivity tensor}$$

yields the dipping anisotropy around the y -axis, i.e.,

$$\mathbf{R}_y^T(\theta)\hat{\rho}\mathbf{R}_y(\theta) = \begin{bmatrix} \rho_{xx} & 0 & \rho_{xz} \\ 0 & \rho_{yy} & 0 \\ \rho_{zx} & 0 & \rho_{zz} \end{bmatrix}. \text{ Although Eq. (2) has no}$$

\mathbf{R}_y , the product $\mathbf{R}_z(90^\circ)\mathbf{R}_x(\theta)\mathbf{R}_z(-90^\circ)$ is equal to \mathbf{R}_y . The influence on the surface responses from \mathbf{R}_y is therefore equivalent to the influence from ρ_{xx} , ρ_{yy} , ρ_{zz} and $\rho_{xz} - \rho_{zx}$.

Here, we conducted similar experiments to those in the dipping anisotropy around x -axis case. The results, which are similar to those in Figs. 5 and 6 of section "The \mathbf{R}_x dipping anisotropy", are summarized in Fig. 8a and b, respectively, while those which are similar to Fig. 7 are given in Fig. 9. Since most of the results obtained in this section are just the opposite of those in section "The \mathbf{R}_x dipping anisotropy", we just give a summary here.

The effect of \mathbf{R}_y

We first investigate the influence of \mathbf{R}_y around y -axis on the surface responses. The surface plots of the $Z_{ij}^{\text{inf}}(s)$ and $T_i^{\text{edge}}(s)$ indices for $\mathbf{R}_y^T(45^\circ)\hat{\rho}_x\mathbf{R}_y(45^\circ)$ are shown in

$$\text{Fig. 8a when } \hat{\rho}_x = \begin{bmatrix} 500 & 0 & 0 \\ 0 & 50 & 0 \\ 0 & 0 & 50 \end{bmatrix}. \text{ Figure 8a shows that}$$

\mathbf{R}_y has stronger effect on Z_{xy} above and around the 3-D body, and on Z_{yy} and T_y around the edges and corners of the 3-D body. The strong influence on the Z_{xy} , Z_{yy} and T_y responses from \mathbf{R}_y is confirmed by the overall Z_{ij}^{inf} and T_i^{edge} indices in Fig. 8b which is in the opposite to those from \mathbf{R}_x (Fig. 6) but similar to the strong influence from ρ_x in the axial cases (section "The axial anisotropy", Fig. 4a and d). However, in this case, the contribution is simply from the combination of ρ_{xx} , ρ_{yy} , ρ_{zz} and $\rho_{xz} - \rho_{zx}$.

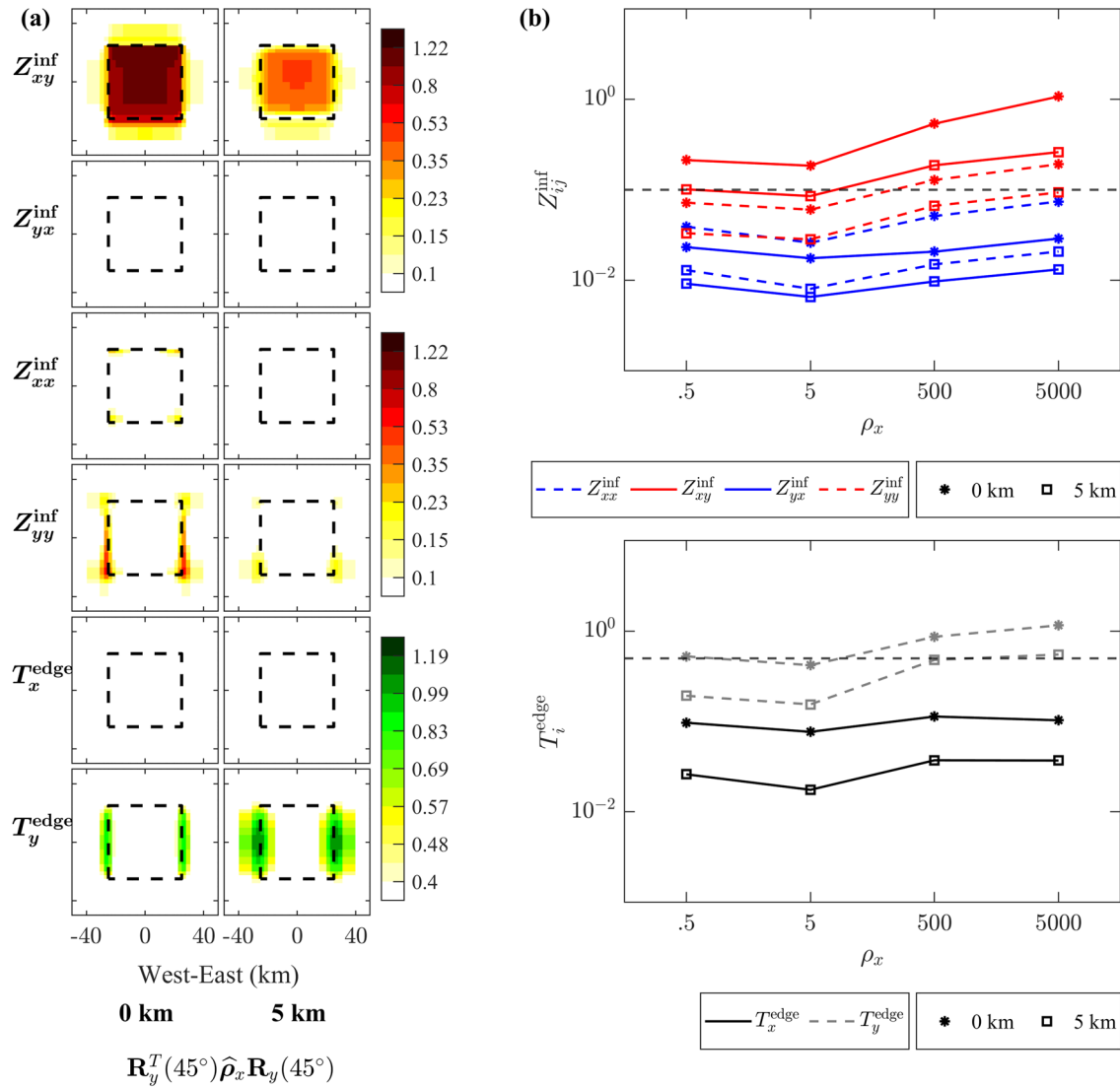


Fig. 8 a The surface logarithmic plot of $Z_{xy}^{inf}(s)$, $Z_{yx}^{inf}(s)$, $Z_{xx}^{inf}(s)$, and $Z_{yy}^{inf}(s)$, and $T_x^{edge}(s)$, and $T_y^{edge}(s)$ at all 484 stations from top to bottom rows, respectively, obtained when the 3-D anisotropic body in Fig. 1 (shown as a dashed line) is assigned with $\mathbf{R}_y^T(45^\circ)\hat{\rho}_x\mathbf{R}_y(45^\circ)$ and buried at the

surface (0 km), and at a depth of 5 km, given $\hat{\rho}_x = \begin{bmatrix} 500 & 0 & 0 \\ 0 & 50 & 0 \\ 0 & 0 & 50 \end{bmatrix}$. b Logarithmic plots of Z_{xx}^{inf} , Z_{yy}^{inf} , Z_{xy}^{inf} , Z_{yx}^{inf} , T_x^{edge} , and T_y^{edge} with

$\mathbf{R}_y^T(45^\circ)\hat{\rho}_x\mathbf{R}_y(45^\circ)$, when $\hat{\rho}_x = \begin{bmatrix} \rho_x & 0 & 0 \\ 0 & 50 & 0 \\ 0 & 0 & 50 \end{bmatrix}$ with ρ_x equaling 0.5, 5, 500, and 5000 Ω -m as shown on the x-axis

The effect of each of ρ_{xx} , ρ_{yy} , ρ_{zz} and $\rho_{xz} - \rho_{zx}$

We then explore the influence from ρ_{xx} , ρ_{yy} , ρ_{zz} and $\rho_{xz} - \rho_{zx}$, one by one, as with the experiments in section "The \mathbf{R}_x dipping anisotropy". Here, ρ_{xx} , ρ_{zz} , and $\rho_{xz} - \rho_{zx}$ must satisfy $\rho_{zz}\rho_{xx} > \rho_{xz}^2$, and all indices are with reference to $\mathbf{R}_y^T(45^\circ)\hat{\rho}_x\mathbf{R}_y(45^\circ)$.

Given $\hat{\rho}_x = \begin{bmatrix} 500 & 0 & 0 \\ 0 & 50 & 0 \\ 0 & 0 & 50 \end{bmatrix}$, then $\mathbf{R}_y^T(45^\circ)\hat{\rho}_x\mathbf{R}_y(45^\circ) = \begin{bmatrix} 275 & 0 & 225 \\ 0 & 50 & 0 \\ 225 & 0 & 275 \end{bmatrix}$ consisting of all

terms ρ_{xx} , ρ_{yy} , ρ_{zz} and $\rho_{xz} - \rho_{zx}$ from \mathbf{R}_y . To see the effect of each of these elements on the surface responses, we first vary ρ_{xx} while other terms are fixed, i.e.,

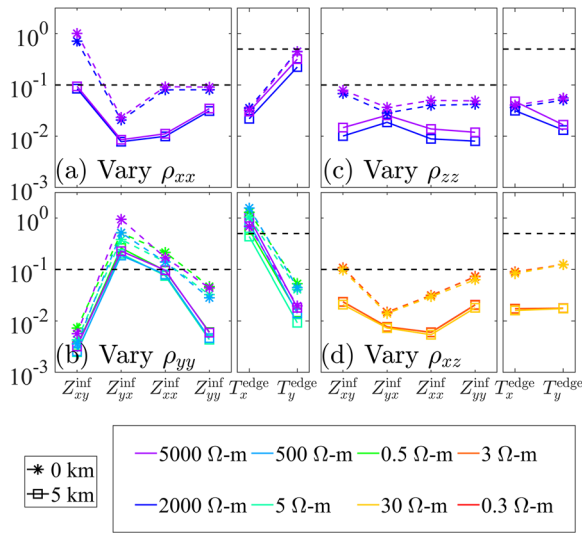


Fig. 9 The logarithmic plots of Z_{xy}^{inf} , Z_{yx}^{inf} , Z_{xx}^{inf} , Z_{yy}^{inf} , and T_x^{edge} , and T_y^{edge} on the x-axis for the case of $\mathbf{R}_y^T(45^\circ)\hat{\rho}_x\mathbf{R}_y(45^\circ)$ equaling **a**

$$\begin{bmatrix} \rho_{xx} & 0 & 225 \\ 0 & 500 & 0 \\ 225 & 0 & 275 \end{bmatrix} \text{ with } \rho_{xx} = 2000 \text{ and } 5000 \text{ } \Omega\text{-m, } \mathbf{b} \begin{bmatrix} 275 & 0 & 225 \\ 0 & \rho_{yy} & 0 \\ 225 & 0 & 275 \end{bmatrix}$$

$$\text{with } \rho_{yy} = 0.5, 5, 500 \text{ and } 5000 \text{ } \Omega\text{-m, } \mathbf{c} \begin{bmatrix} 275 & 0 & 225 \\ 0 & 50 & 0 \\ 225 & 0 & \rho_{zz} \end{bmatrix} \text{ with } \rho_{zz} =$$

$$2000 \text{ and } 5000 \text{ } \Omega\text{-m, and } \mathbf{d} \begin{bmatrix} 275 & 0 & \rho_{xz} \\ 0 & 50 & 0 \\ \rho_{xz} & 0 & 275 \end{bmatrix} \text{ with } \rho_{xz} = 0.3, 3 \text{ and } 30$$

$$\Omega\text{-m. The indices are all with reference to } \mathbf{R}_y^T(45^\circ)\hat{\rho}_x\mathbf{R}_y(45^\circ) = \begin{bmatrix} 275 & 0 & 225 \\ 0 & 50 & 0 \\ 225 & 0 & 275 \end{bmatrix}$$

$$\begin{bmatrix} \rho_{xx} & 0 & 225 \\ 0 & 50 & 0 \\ 225 & 0 & 275 \end{bmatrix}. \text{ The indices to indicate the influence of } \rho_{xx}$$

are measured with respect to $\mathbf{R}_y^T(45^\circ)\hat{\rho}_x\mathbf{R}_y(45^\circ)$ and are shown in Fig. 9a, when $\rho_{xx} = 2000$ and $5000 \text{ } \Omega\text{-m}$. Simi-

larly, the indices for the effect of $\begin{bmatrix} 275 & 0 & 225 \\ 0 & \rho_{yy} & 0 \\ 225 & 0 & 275 \end{bmatrix}$,

$$\begin{bmatrix} 275 & 0 & 225 \\ 0 & 50 & 0 \\ 225 & 0 & \rho_{zz} \end{bmatrix} \text{ and } \begin{bmatrix} 275 & 0 & \rho_{xz} \\ 0 & 50 & 0 \\ \rho_{xz} & 0 & 275 \end{bmatrix} \text{ are shown in Fig. 9b–d,}$$

respectively, when $\rho_{yy} = 0.5, 5, 500$ and $5000 \text{ } \Omega\text{-m}$, $\rho_{zz} = 2000$ and $5000 \text{ } \Omega\text{-m}$, and $\rho_{xz} = 0.3, 3$ and $30 \text{ } \Omega\text{-m}$.

The results from varying only ρ_{xx} (Fig. 9a) or ρ_{yy} (Fig. 9b) while fixing the other elements, in this section, are in the opposite of the results in section "The \mathbf{R}_x dipping anisotropy". Varying only ρ_{xx} clearly affects just the strong Z_{xy} , Z_{yy} and T_y responses (Fig. 9a), as with the effect from \mathbf{R}_y , but varying ρ_{yy} has no effect on these strong responses but does affect the weak Z_{yx} , Z_{xx} and T_x responses (Fig. 9b) from \mathbf{R}_y . As in section "The \mathbf{R}_x

dipping anisotropy", unexpected results occur when varying the ρ_{zz} (Fig. 9c) or ρ_{xz} (Fig. 9d) elements which show a relatively low influence on all responses. This indicates that ρ_{zz} and ρ_{xz} contribute less to the strong influence responses Z_{xy} , Z_{yy} and T_y from \mathbf{R}_y (Fig. 8) than ρ_{xx} , and can possibly be omitted as will be discussed in the next section.

The azimuthal anisotropy

To obtain the azimuthal anisotropic 3-D body, we applied \mathbf{R}_z to both sides of the axial resistivity tensor, i.e.,

$$\mathbf{R}_z^T(\theta)\hat{\rho}\mathbf{R}_z(\theta) = \begin{bmatrix} \rho_{xx} & \rho_{xy} & 0 \\ \rho_{yx} & \rho_{yy} & 0 \\ 0 & 0 & \rho_{zz} \end{bmatrix}. \text{ The influence on the}$$

surface responses from \mathbf{R}_z is therefore equivalent to the influence from combinations of ρ_{xx} , ρ_{yy} , ρ_{zz} and $\rho_{xy} - \rho_{yx}$.

The effect of \mathbf{R}_z

To see the influence from \mathbf{R}_z or the combinations of ρ_{xx} , ρ_{yy} , ρ_{zz} and $\rho_{xy} - \rho_{yx}$, we performed $\mathbf{R}_z^T(\theta)\hat{\rho}\mathbf{R}_z(\theta)$ with various θ on the 3-D anisotropic body (Fig. 1) where

$$\hat{\rho}_x = \begin{bmatrix} \rho_x & 0 & 0 \\ 0 & 50 & 0 \\ 0 & 0 & 50 \end{bmatrix} (\Omega\text{-m}) \text{ with } \rho_x \text{ at } 0.5, 5, 500, \text{ and } 5000$$

$\Omega\text{-m}$. The station influences and edge effects for the case where $\rho_x = 500 \text{ } \Omega\text{-m}$ and $\theta = 45^\circ$ are shown in Fig. 10a where the 3-D anisotropic body is at the surface and 5 km deep, respectively. Figure 10b shows the overall influence and edge effect for all of these values of ρ_x .

Interestingly, the action from \mathbf{R}_z , regardless of θ and ρ_x , has a strong impact on all kinds of responses (Fig. 10a and b), unlike the axial anisotropy (section "The axial anisotropy") or the dipping anisotropy (section "The \mathbf{R}_x dipping anisotropy" and "The \mathbf{R}_y dipping anisotropy") where ρ_x , ρ_y , \mathbf{R}_x , and \mathbf{R}_y affect only half of the responses. Previously, the direct effects on Z_{xx} and Z_{yy} of the axial or dipping anisotropy can only be seen just around the edges and corners (Figs. 3c–f, 5, and 8a). Here, the effects from \mathbf{R}_z on Z_{xx} and Z_{yy} are much stronger and cover the whole of the 3-D body (Fig. 10a) with a magnitude close to those of Z_{xy} and Z_{yx} . This is confirmed by the overall Z_{xx}^{inf} , Z_{yy}^{inf} , Z_{xy}^{inf} , Z_{yx}^{inf} , T_x^{edge} , and T_y^{edge} indices in Fig. 10b in which all Z_{ij}^{inf} and T_i^{edge} indices obtained from the structure at the same buried depths are shown at similar levels. For other θ , the levels of the impact on all responses are similar to those in Fig. 10b but with different amplitudes. It is therefore clear that the action of \mathbf{R}_z affects all responses confirming the studies of Kong et al. (2018).

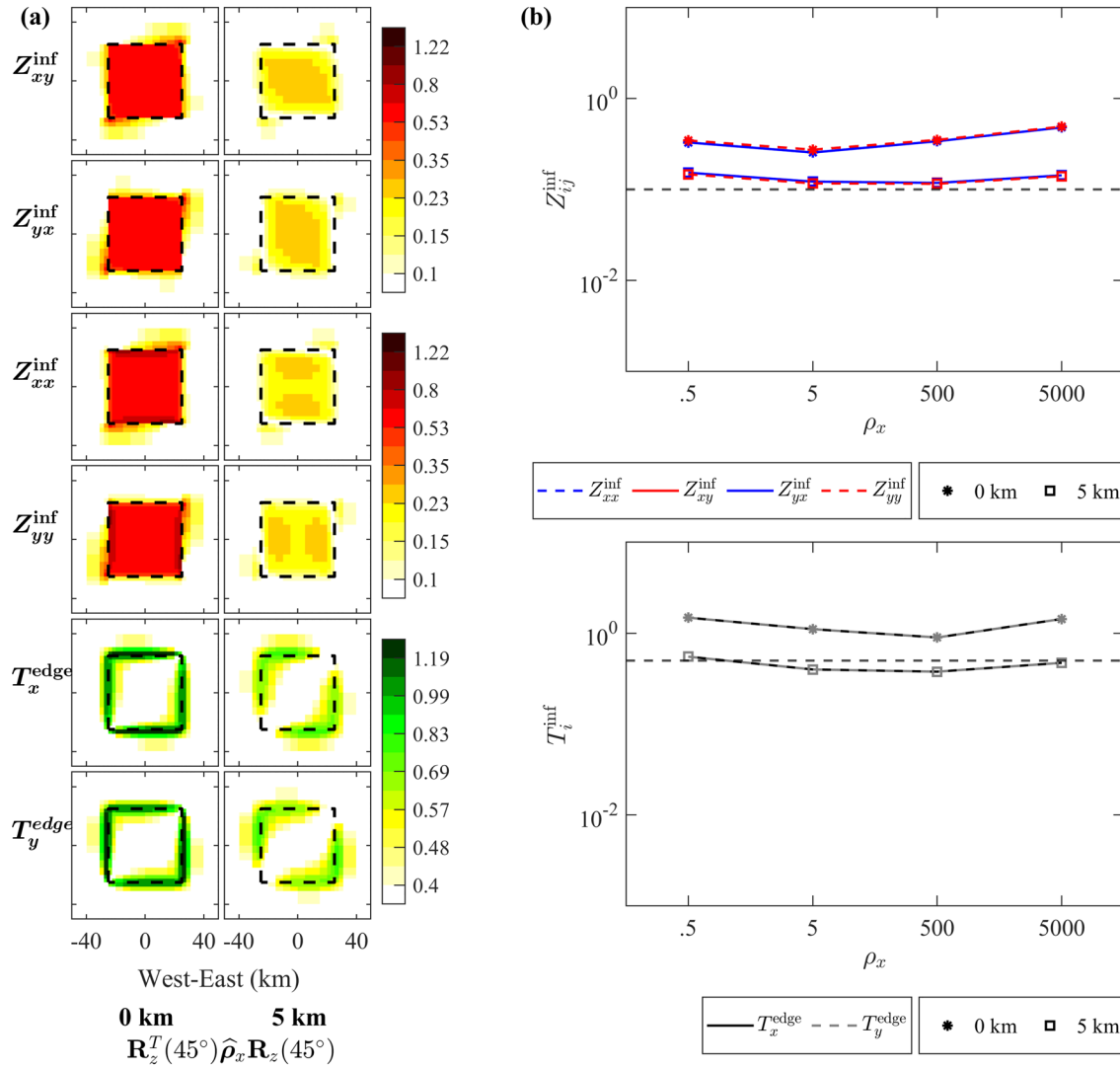


Fig. 10 a The surface logarithmic plot of $Z_{xy}^{inf}(s)$, $Z_{yx}^{inf}(s)$, $Z_{xx}^{inf}(s)$, and $Z_{yy}^{inf}(s)$, and $T_x^{edge}(s)$, and $T_y^{edge}(s)$ at all 484 stations from top to bottom rows, respectively, obtained when the 3-D anisotropic body in Fig. 1 (shown as a dashed line) is assigned with $\mathbf{R}_z^T(45^\circ)\hat{\rho}_x\mathbf{R}_z(45^\circ)$ and buried at the

surface (0 km), and at a depth of 5 km, given $\hat{\rho}_x = \begin{bmatrix} 500 & 0 & 0 \\ 0 & 50 & 0 \\ 0 & 0 & 50 \end{bmatrix}$. b Logarithmic plots of Z_{xx}^{inf} , Z_{yy}^{inf} , Z_{xy}^{inf} , Z_{yx}^{inf} , T_x^{edge} , and T_y^{edge} with

$\mathbf{R}_z^T(45^\circ)\hat{\rho}_x\mathbf{R}_z(45^\circ)$, when $\hat{\rho}_x = \begin{bmatrix} \rho_x & 0 & 0 \\ 0 & 50 & 0 \\ 0 & 0 & 50 \end{bmatrix}$ with ρ_x equaling 0.5, 5, 500, and 5000 Ω -m shown on the x-axis

The effect of each of ρ_{xx} , ρ_{yy} , ρ_{zz} and $\rho_{xy} - \rho_{yx}$

Here, we further investigate the role of each of ρ_{xx} , ρ_{yy} , ρ_{zz} and $\rho_{xy} - \rho_{yx}$ from the 3-D azimuthal anisotropic body influence on the surface responses. As in sections "The \mathbf{R}_x dipping anisotropy" and "The \mathbf{R}_y dipping anisotropy", here, we must have $\rho_{xx}\rho_{yy} < \rho_{xy}^2$, and each element is varied while keeping the other elements constant.

Given $\hat{\rho}_x = \begin{bmatrix} 500 & 0 & 0 \\ 0 & 50 & 0 \\ 0 & 0 & 50 \end{bmatrix}$, then

$$\mathbf{R}_z^T(45^\circ)\hat{\rho}_x\mathbf{R}_z(45^\circ) = \begin{bmatrix} 275 & 225 & 0 \\ 225 & 275 & 0 \\ 0 & 0 & 50 \end{bmatrix} \text{ consisting with all}$$

terms ρ_{xx} , ρ_{yy} , ρ_{zz} and $\rho_{xy} - \rho_{yx}$ from \mathbf{R}_z . To see the effect of each of these elements on the surface responses, we first vary ρ_{xx} while other terms are fixed, i.e.,

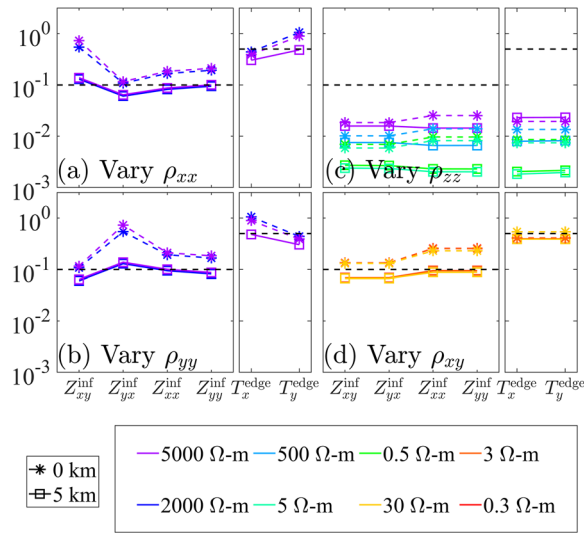


Fig. 11 The logarithmic plots of Z_{xx}^{inf} , Z_{yy}^{inf} , Z_{xy}^{inf} , Z_{yx}^{inf} , T_x^{edge} , and T_y^{edge} on the x-axis for the case of $\mathbf{R}_z^T(45^\circ) \hat{\rho}_x \mathbf{R}_z(45^\circ)$ equaling **a**

$$\begin{bmatrix} \rho_{xx} & 225 & 0 \\ 225 & 275 & 0 \\ 0 & 0 & 50 \end{bmatrix} \text{ with } \rho_{xx} = 2000 \text{ and } 5000 \text{ } \Omega\text{-m, b } \begin{bmatrix} 275 & 225 & 0 \\ 225 & \rho_{yy} & 0 \\ 0 & 0 & 50 \end{bmatrix}$$

$$\text{with } \rho_{yy} = 2000 \text{ and } 5000 \text{ } \Omega\text{-m, c } \begin{bmatrix} 275 & 225 & 0 \\ 225 & 275 & 0 \\ 0 & 0 & \rho_{zz} \end{bmatrix} \text{ with } \rho_{zz} = 0.5, 5,$$

$$500 \text{ and } 5000 \text{ } \Omega\text{-m, and d } \begin{bmatrix} 275 & \rho_{xy} & 0 \\ \rho_{xy} & 275 & 0 \\ 0 & 0 & 50 \end{bmatrix} \text{ with } \rho_{xy} = 0.3, 3 \text{ and } 30$$

$\Omega\text{-m}$. The indices are all with reference to $\mathbf{R}_z^T(45^\circ) \hat{\rho}_x \mathbf{R}_z(45^\circ)$

$$= \begin{bmatrix} 275 & 225 & 0 \\ 225 & 275 & 0 \\ 0 & 0 & 50 \end{bmatrix}$$

$$\begin{bmatrix} \rho_{xx} & 225 & 0 \\ 225 & 275 & 0 \\ 0 & 0 & 50 \end{bmatrix}. \text{ The } Z_{xx}^{\text{inf}}, Z_{yy}^{\text{inf}}, Z_{xy}^{\text{inf}}, Z_{yx}^{\text{inf}}, T_x^{\text{edge}}, \text{ and } T_y^{\text{edge}}$$

indices to indicate the influence of ρ_{xx} measured with respect to $\mathbf{R}_z^T(45^\circ) \hat{\rho}_x \mathbf{R}_z(45^\circ)$ are shown in Fig. 11a when $\rho_{xx} = 2000$ and $5000 \text{ } \Omega\text{-m}$. Similarly, the indices for the

$$\text{effect of } \begin{bmatrix} 275 & 225 & 0 \\ 225 & \rho_{yy} & 0 \\ 0 & 0 & 50 \end{bmatrix}, \begin{bmatrix} 275 & 225 & 0 \\ 225 & 275 & 0 \\ 0 & 0 & \rho_{zz} \end{bmatrix} \text{ and}$$

$$\begin{bmatrix} 275 & \rho_{xy} & 0 \\ \rho_{xy} & 275 & 0 \\ 0 & 0 & 50 \end{bmatrix} \text{ are shown in Fig. 11b–d, respectively,}$$

when $\rho_{yy} = 2000$ and $5000 \text{ } \Omega\text{-m}$, $\rho_{zz} = 0.5, 5, 500$ and $5000 \text{ } \Omega\text{-m}$, and $\rho_{xy} = 0.3, 3$ and $30 \text{ } \Omega\text{-m}$.

A combination of ρ_{xx} , ρ_{yy} , ρ_{zz} and $\rho_{xy} - \rho_{yx}$ of \mathbf{R}_z has a strong influence on all responses (Fig. 10). In our experiments, varying ρ_{xx} (Fig. 11a), ρ_{yy} (Fig. 11b) or ρ_{xy} (Fig. 11d) shows strong effects on all of the responses, especially when the 3-D anisotropic body is close to the surface. In contrast, varying ρ_{zz} (Fig. 11c) shows a very weak influence on all responses, as seen in most of our

previous studies. Thus, in this experiment, a combination of just ρ_{xx} , ρ_{yy} and ρ_{xy} strongly influences all responses.

Discussion and conclusions

In isotropic MT inversion, we usually use all response types and components, Z_{xy} , Z_{yx} , Z_{xx} , Z_{yy} , T_x and T_y (or just the off-diagonal tensor, Z_{xy} and Z_{yx} , as a minimum) as inputs to invert for the single parameter, ρ , the isotropic resistivity. For the anisotropic case, the medium is associated with six parameters, either the tensor ρ_{xx} , ρ_{yy} , ρ_{zz} , ρ_{xy} , ρ_{xz} , and ρ_{yz} elements, or the ρ_x , ρ_y , and ρ_z and the anisotropy angles α_S , α_D , and α_L , via \mathbf{R}_z and \mathbf{R}_x . The six-fold increase in the number of parameters has raised the CPU time and memory usage even with current modern computer technology. This makes the general anisotropic inversion less practical unless performing the inversion on a high-end parallel computing machine (see Kong et al. 2021; Rong et al. 2022).

If prior geological or geophysical information is known, one might prefer to simplify the medium to just the azimuthal anisotropy (via \mathbf{R}_z) or the dipping anisotropy (via \mathbf{R}_x) or the axial anisotropy. In the past decade, many developers (e.g., Wang et al. 2017; Cao et al. 2018; Luo et al. 2020) have successfully completed the axial anisotropic inversion to search for the three principal resistivities, ρ_x , ρ_y , and ρ_z , as this is more practical for the current computational resources. However, Kong et al. (2021) and Rong et al. (2022) pointed out the limitations for the axial anisotropic inversion if there is an anisotropic strike.

Another ambiguity could occur for the inversion of either the azimuthal anisotropy $\mathbf{R}_z^T(\theta) \hat{\rho} \mathbf{R}_z(\theta)$ or the dipping anisotropy $\mathbf{R}_x^T(\theta) \hat{\rho} \mathbf{R}_x(\theta)$ as we found in our experiments. For example, for azimuthal anisotropy, if the 3-D anisotropic body in Fig. 1 has an axial resistivity tensor,

$$\hat{\rho}_{xy} = \begin{bmatrix} \rho_x & 0 & 0 \\ 0 & \rho_y & 0 \\ 0 & 0 & \rho_z \end{bmatrix} \text{ with strike angle } \alpha_S, \text{ we found that}$$

$\mathbf{R}_z^T(\alpha_S) \hat{\rho}_{xy} \mathbf{R}_z(\alpha_S)$ yields exactly the same responses to

$$\mathbf{R}_z^T(90^\circ + \alpha_S) \hat{\rho}_{yx} \mathbf{R}_z(90^\circ + \alpha_S), \text{ when } \hat{\rho}_{yx} = \begin{bmatrix} \rho_y & 0 & 0 \\ 0 & \rho_x & 0 \\ 0 & 0 & \rho_z \end{bmatrix},$$

if there is no constraint on the angle.

All the studies of the influence from each anisotropic case to the responses from previous section are summarized in Fig. 12. Here, based on these studies (Fig. 12), instead of the conventional anisotropic inversions, we introduce two new processes to perform the anisotropic inversion as outlined in Fig. 13. First in section "The exclusion of the weak influence ρ_{zz} , $\rho_{xz} - \rho_{zx}$ and $\rho_{yz} - \rho_{zy}$ elements", we explain why ρ_{zz} , ρ_{xz} and ρ_{yz} become unnecessary and can be excluded. In section "Two decoupled ρ_x -mode and ρ_y -mode anisotropic

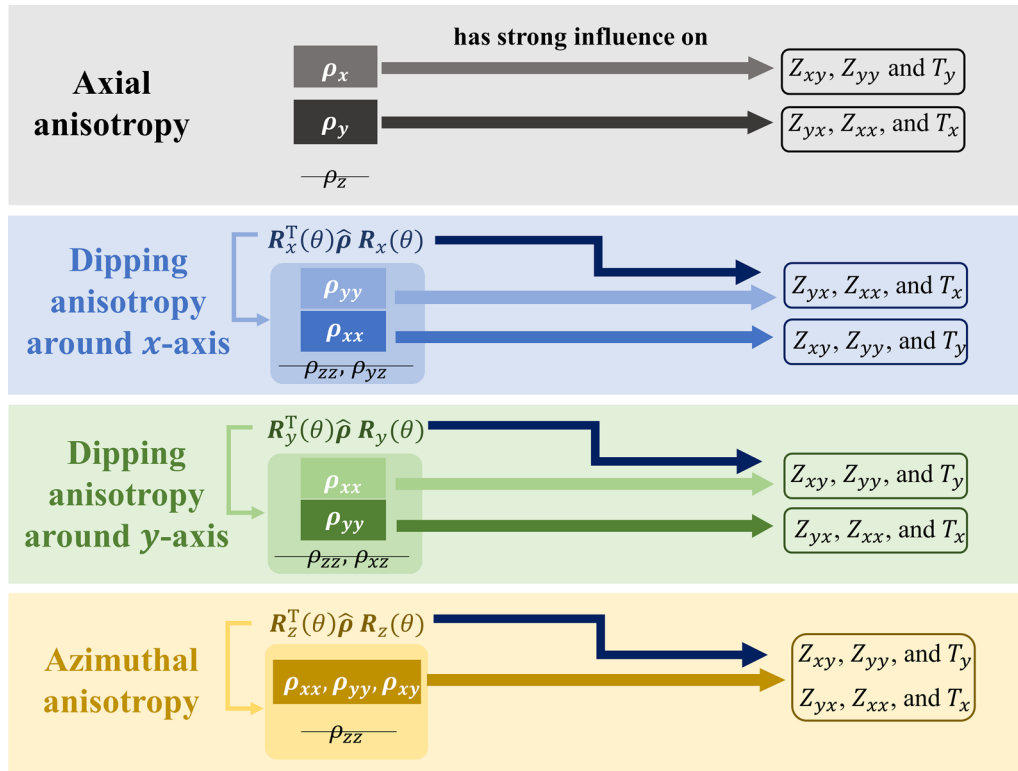


Fig. 12 A one-page summary of the influence of the resistivity elements on the surface responses from the four anisotropic cases in sections. "The axial anisotropy"—"The azimuthal anisotropy"

inversions", we separate the axial anisotropic inversion into two independent or decoupled modes: the ρ_x -mode inversion and the ρ_y -mode inversion. In section "Reduced coupled azimuthal anisotropic inversion", we show that the general anisotropic inversion with six output parameters can be simplified to the reduced coupled azimuthal anisotropic inversion with just three outputs. In section "Criteria to choose between decoupled and coupled inversion modes", we discuss the criteria to choose whether to perform the decoupled or the coupled inversions.

The exclusion of the weak influence $\rho_{zz}, \rho_{xz} - \rho_{zx}$ and $\rho_{yz} - \rho_{zy}$ elements

The strong influence elements, like ρ_x and ρ_y , result in a significantly difference to the inversion RMS misfits for a range of resistivity values, particularly if Z_{xy} and Z_{yx} are the major responses. It is then straightforward to understand why past anisotropic inversion can recover the correct values of ρ_x and ρ_y (e.g., Wang et al. 2017; Cao et al. 2018; Luo et al. 2020; Kong et al. 2021; Rong et al. 2022). In contrast, the weak influence elements have little effect on the misfits regardless of the resistivity values. This makes it difficult for the inversion to recover these weak influence elements.

According to our studies, in the axial anisotropic case (section "The axial anisotropy") and both dipping anisotropic cases (section "The R_x dipping anisotropy", and "The R_y dipping anisotropy"), and the azimuthal anisotropic case (section "The azimuthal anisotropy"), ρ_z (or ρ_{zz}) shows a very weak influence on all responses (summarized in Fig. 12). Both dipping anisotropic studies (section "The R_x dipping anisotropy" and "The R_y dipping anisotropy") also suggest that both ρ_{yz} in the case of R_x and ρ_{xz} in the case of R_y yield relatively weak influence responses, particularly on Z_{yx} and Z_{xy} , respectively.

Because of the low contribution to the responses of the ρ_{zz}, ρ_{yz} and ρ_{xz} elements, this makes it difficult for any anisotropic inversions to recover them. This was proven as many previous anisotropic inversions fail to resolve the ρ_z elements (e.g., Wang et al. 2017; Cao et al. 2018; Luo et al. 2020; Kong et al. 2021; Rong et al. 2022). In a recently developed inversion technique for the dipping anisotropy case, Rong et al. (2022) found that they can resolve just the two horizontal resistivities, ρ_{xx} , and ρ_{yy} , but not the dipping angle α_D . The dipping angle through R_x and R_y corresponds to the contribution from ρ_{yz} and ρ_{xz} , respectively. This confirms that these weak influence elements ρ_{yz} and ρ_{xz} cannot be well resolved.

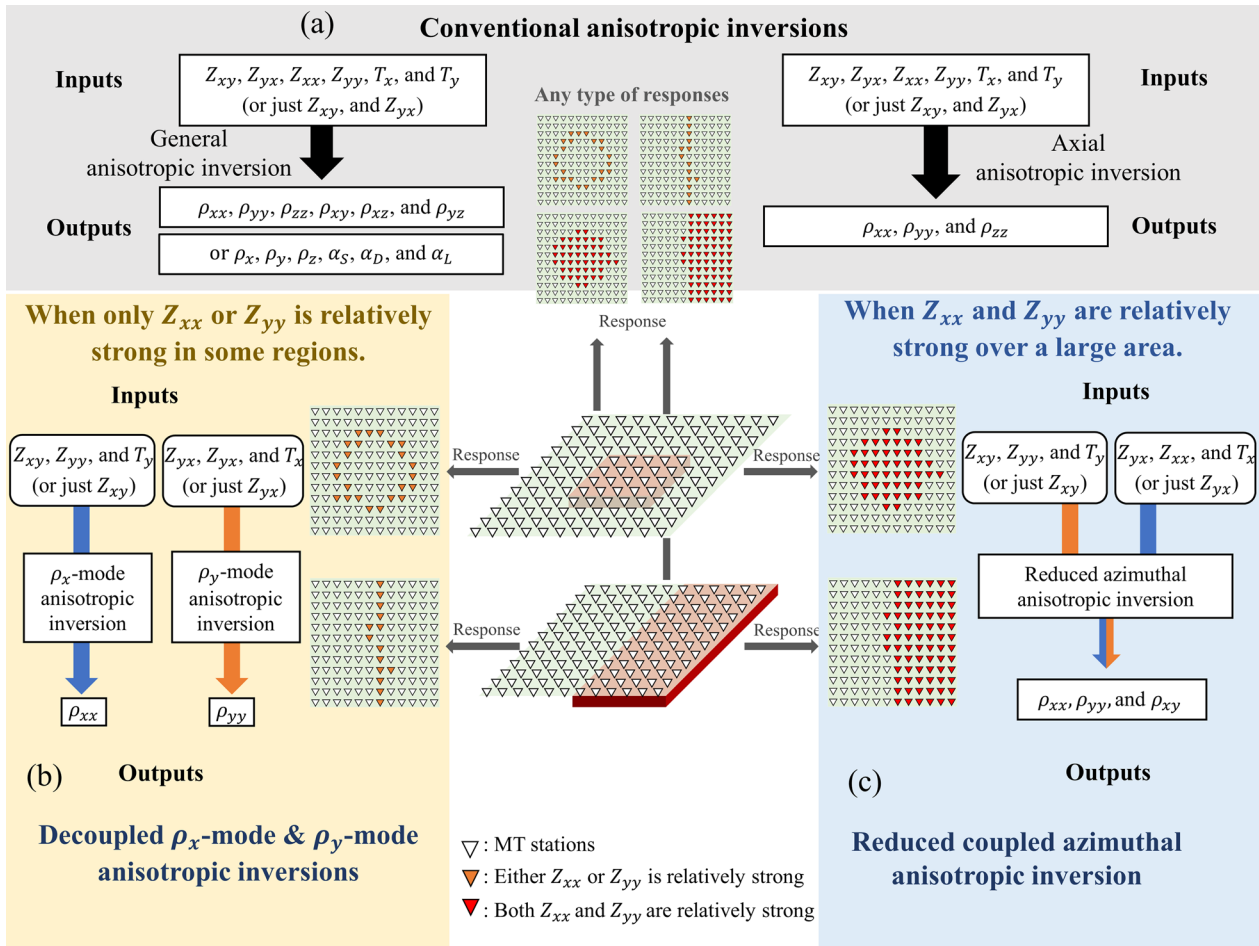


Fig. 13 A one-page summary of **a** the conventional methods and our two new designed processes, **b** the decoupled ρ_x —mode and ρ_y —mode anisotropic inversion, and **c** the reduced coupled azimuthal anisotropic inversion

With our studies and the previous inversion experiments, we therefore propose excluding these weak ρ_{zz} , ρ_{yz} and ρ_{xz} elements from any anisotropic inversion. The influence on the responses from these elements would be even lower when the 3-D anisotropy body is at greater depth, or the acquired MT stations are not located around the edges or corners of the 3-D anomaly. In addition, if the observed data are noisy with large error bars, the noise would overwhelm these weak influences. With these factors, the exclusion of these weak influence elements in any kind of anisotropic inversion is reasonable and practical.

Two decoupled ρ_x -mode and ρ_y -mode anisotropic inversions

In the previous section, we recommended removing the weak influence elements (ρ_{zz} , ρ_{xz} and ρ_{yz}) from the axial

or dipping anisotropic inversion. This, then, leaves us with just the ρ_x (or ρ_{xx}) and ρ_y (or ρ_{yy}) for these cases. Recall that in our axial (section "The axial anisotropy"), and dipping (sections "The R_x dipping anisotropy" and "The R_y dipping anisotropy") anisotropic studies, ρ_x (or ρ_{xx}) has a strong influence on Z_{xy} , Z_{yy} , and T_y , and a very weak influence on Z_{yx} , Z_{xx} , and T_x , while ρ_y (or ρ_{yy}) has opposite the influence, strong on Z_{yx} , Z_{xx} , and T_x and very weak on Z_{xy} , Z_{yy} , and T_y . This is summarized in Fig. 12.

Because ρ_x has a relatively low influence on Z_{yx} , Z_{xx} and T_x , including these responses as inputs for conventional axial anisotropic inversion will not have much effect on the RMS misfits. This is for the same reason that ρ_y has a low influence on Z_{xy} , Z_{yy} and T_y . We therefore recommend decoupling the axial and dipping anisotropy systems into two independent modes for inversion: the ρ_x -mode anisotropic inversion and the ρ_y -mode anisotropic

inversion (Fig. 13). After decoupling, the ρ_x -mode inversion requires only Z_{xy} , Z_{yy} and T_y (or just Z_{xy} as a minimum) as inputs to invert for the ρ_x element, while the ρ_y -mode inversion requires only Z_{yx} , Z_{xx} and T_x (or just Z_{yx} as a minimum) as inputs to invert for the ρ_y element (Fig. 13).

By separation, we can reduce the amount of computational resources required to gain a better inversion performance. For example, the conventional axial or general anisotropic inversion (e.g., Wang et al. 2017; Cao et al. 2018; Luo et al. 2020; Kong et al. 2021; Rong et al. 2022) requires all responses (6 responses or 2 as minimum) as inputs, while either the ρ_x -mode inversion or the ρ_y -mode inversion requires just 3 responses (or 1 as a minimum) for each mode (see Fig. 13). The outputs are also down from 3 principal resistivities in the conventional axial inversion (e.g., Wang et al. 2017; Cao et al. 2018; Luo et al. 2020; Kong et al. 2021; Rong et al. 2022) or 4 elements in the dipping anisotropy inversion (e.g., Rong et al. 2022) to just 1 resistivity for each decoupled mode inversion (Fig. 13). Because the inputs and outputs are lower, memory requirements are significantly reduced as well as the computational times for the inversion. In addition, since both ρ_x -mode and the ρ_y -mode inversions are independent of each other, they can be inverted simultaneously on a parallel machine.

In section "Criteria to choose between decoupled and coupled inversion modes", we discuss the criteria for when to apply these two decoupled inversion modes.

Reduced coupled azimuthal anisotropic inversion

For the azimuthal anisotropy (Figs. 10 and 11), the action $\mathbf{R}_z^T(\theta)\hat{\rho}\mathbf{R}_z(\theta)$ is a result of a combination of ρ_{xx} , ρ_{yy} and ρ_{xy} (excluding a weak ρ_{zz} element). The strong influence ρ_{xx} and ρ_{yy} elements provide an impact on all responses, Z_{xy} , Z_{yx} , Z_{xx} , Z_{yy} , T_x and T_y . The contribution from the off-diagonal ρ_{xy} elements help further increase the magnitudes of the Z_{xx} , Z_{yy} , T_x and T_y responses everywhere over the 3-D anisotropic body as shown in Figs. 10 and 11. We therefore cannot separate the azimuthal anisotropy into two modes as in the previous section but can only exclude the ρ_{zz} element. As ρ_{zz} is excluded, we refer to this case as the reduced coupled azimuthal anisotropy.

The general form of the anisotropy tensor is
$$\begin{bmatrix} \rho_{xx} & \rho_{xy} & \rho_{xz} \\ \rho_{yx} & \rho_{yy} & \rho_{yz} \\ \rho_{zx} & \rho_{zy} & \rho_{zz} \end{bmatrix}$$
 as in (1). Since ρ_{zz} , ρ_{xz} and ρ_{yz} can be eliminated, this leaves us with only the strong and

coupled ρ_{xx} , ρ_{yy} , and ρ_{xy} elements, i.e., $\approx \begin{bmatrix} \rho_{xx} & \rho_{xy} & 0 \\ \rho_{yx} & \rho_{yy} & 0 \\ 0 & 0 & \rho_{zz} \end{bmatrix}$.

Here, ρ_{zz} is required just for the completion of the forward modeling, but is not necessarily needed as an inversion parameter. We therefore recommend that the reduced coupled azimuthal anisotropic inversion is used instead of the general anisotropic inversion. This design reduces the output parameters from six to just three, ρ_{xx} , ρ_{yy} , and ρ_{xy} , or ρ_{xx} , ρ_{yy} , and $\mathbf{R}_z(\alpha_S)$. With the halving in the number of outputs, we can make significant saving in CPU time and memory, but still gain a useful and interpretable inverted anisotropic model.

Although Kong et al. (2021) and Rong et al. (2022) attempt to invert all anisotropic parameters, they found that they can accurately recover just ρ_{xx} , ρ_{yy} , and α_S but not ρ_{zz} , α_D and α_L . Their separate experiments strongly support our recommendations.

Criteria to choose between decoupled and coupled inversion modes

For our proposed recommendations, the criteria to choose which type of anisotropic inversion to perform depend greatly on the (1) the magnitude of the Z_{xx} (and T_x) and/or Z_{yy} (and T_y) responses, and (2) the site distribution of the relatively large magnitude Z_{xx} (and T_x) and/or Z_{yy} (and T_y) responses as summarized in Fig. 13. Since many MT field surveys do not acquire the vertical magnetic field H_z , and Kong et al. (2021) found that the tipper does not help the inversion to recover the anisotropic structure, we put the T_x and T_y in parentheses as optional data.

Figures 3, 5 and 8 demonstrate that in the cases of the axial (Fig. 3) and dipping anisotropy (Figs. 5 and 8), the zones where the large magnitude of Z_{xx} (and T_x) or Z_{yy} (and T_y) (large magnitude corresponding to strong influence for Z_{xx} , Z_{yy} , T_x and T_y , and vice versa) occurs is just around the edges and corners of the 3-D anisotropic body. In contrast, both Z_{xx} and Z_{yy} are large all over the 3-D anisotropic body for the azimuthal anisotropic case (Fig. 10a). We therefore use this observation on Z_{xx} and Z_{yy} (and T_x and T_y) as a criterion to choose which modes to perform the inversion.

For a given data set, assume that (1) the MT stations are well distributed around a large area of investigation; (2) the acquired data, particularly for the Z_{xx} and Z_{yy} (T_x and T_y) responses, is of good quality; (3) no galvanic distortion involved (Rung-Arunwan et al. 2016) and (4) prior geological and geophysical information has suggested the existence of electrical anisotropy.

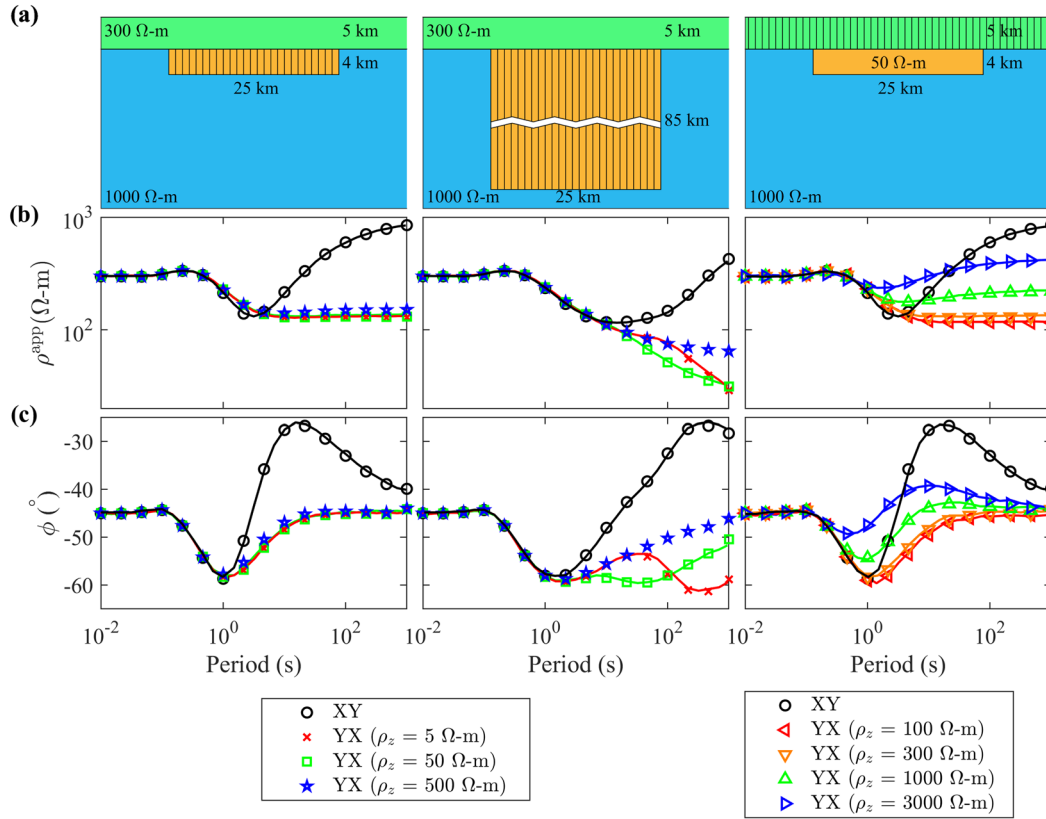


Fig. 14 **a** The three 2-D synthetic models of Pek et al. (2008), **b** their corresponding apparent resistivities and **c** phases. Solid lines are responses digitized from Fig. 3 of Marti (2014). Colored symbols are our calculations for various vertical resistivity values

If Z_{xx} (and T_x) is relatively large and Z_{yy} (and T_y) is relatively small at some sites connecting and forming a narrow stripe or small pattern (Fig. 13b), this indicates that these sites are located around the edges or corners of 3-D anisotropic anomalies and are getting strongly influenced by the ρ_y element (Fig. 12). In contrast, if Z_{yy} (and T_y) is much larger than Z_{xx} (and T_x), this indicates the influence from the ρ_x element (Fig. 12). In these cases, decoupled ρ_x -mode and ρ_y -mode inversions are recommended for this region. In the case where Z_{xx} and Z_{yy} are very low, but anisotropy is necessary, the decoupled mode is also recommended with just Z_{xy} and Z_{yx} as inputs.

If the Z_{xx} and Z_{yy} responses (and T_x and T_y response) have magnitude relatively about the same or just a decade lower than the Z_{xy} and Z_{yx} responses (Fig. 13c), then these sites are strongly influenced by ρ_{xx} , ρ_{yy} , and ρ_{xy} of the 3-D anisotropic anomalies (Fig. 12). In this scenario, a reduced coupled azimuthal anisotropic inversion is recommended.

Usually, obtaining good-quality Z_{xx} , Z_{yy} , T_x and T_y data can be difficult, especially if the MT stations are in noisy area (see Boonchaisuk et al. 2013; Wang et al. 2014; Amatyakul et al. 2015, 2016, 2021). This can therefore

pose an obstacle as including noisy data in the inversion may cause worse results than not including it.

Both processes (Fig. 13) display the conceptual designs from our studies. They still need further validation from either the previous developed anisotropic inversion codes (e.g., Kong et al. 2021; Rong et al. 2022) or any new developments.

Appendices

Appendix A: Implementation of the 3-D anisotropic forward modeling

Given $e^{-i\omega t}$ as the time dependence and using a quasi-stationary approximation, the 2nd order Maxwell's differential equations in the electric field (\mathbf{E}) in an anisotropic medium can be written as:

$$\frac{\partial^2 E_y}{\partial y \partial x} - \frac{\partial^2 E_x}{\partial y^2} - \frac{\partial^2 E_x}{\partial z^2} + \frac{\partial^2 E_z}{\partial z \partial x} = i\omega\mu_0(\sigma_{xx}E_x + \sigma_{xy}E_y + \sigma_{xz}E_z), \quad (7)$$

$$\frac{\partial^2 E_x}{\partial x \partial y} - \frac{\partial^2 E_y}{\partial x^2} - \frac{\partial^2 E_y}{\partial z^2} + \frac{\partial^2 E_z}{\partial z \partial y} = i\omega\mu_0(\sigma_{yx}E_x + \sigma_{yy}E_y + \sigma_{yz}E_z), \quad (8)$$

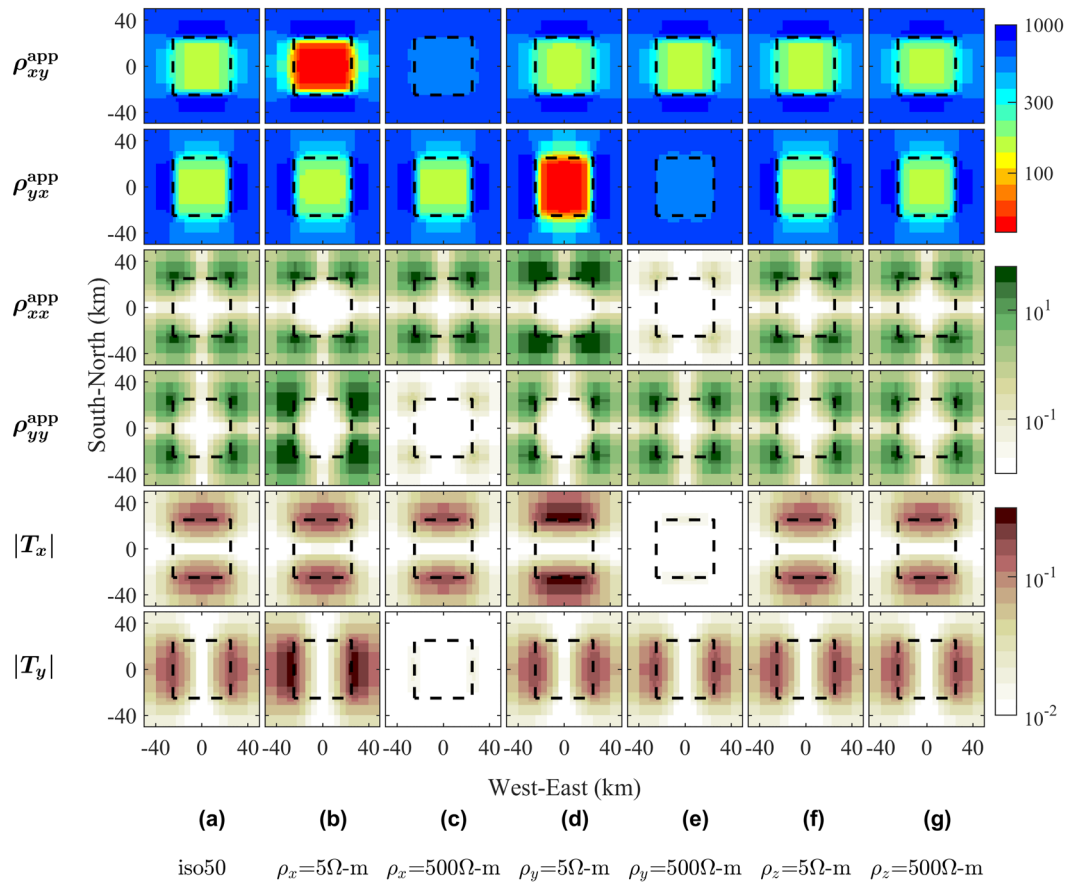


Fig. 15 The surface plots of the apparent resistivities ρ_{xy}^{app} , ρ_{yx}^{app} , ρ_{xx}^{app} , and ρ_{yy}^{app} and the magnitude of the tipper $|T_x|$ and $|T_y|$, respectively, from top to bottom rows, at a period of 10 s from **a** the isotropic case of $\rho = 50 \Omega\text{-m}$ as reference, and axial anisotropic cases when **b** $\rho_x = 5 \Omega\text{-m}$, **c** $\rho_x = 500 \Omega\text{-m}$, **d** $\rho_y = 5 \Omega\text{-m}$, **e** $\rho_y = 500 \Omega\text{-m}$, **f** $\rho_z = 5 \Omega\text{-m}$, and **g** $\rho_z = 500 \Omega\text{-m}$ in the axial anisotropy experiment in section "The axial anisotropy". The dash line marks the boundary of the 3-D body in Fig. 1 where it is buried at 5 km depth

$$\frac{\partial^2 E_x}{\partial x \partial z} - \frac{\partial^2 E_z}{\partial x^2} - \frac{\partial^2 E_x}{\partial y^2} + \frac{\partial^2 E_y}{\partial y \partial z} = i\omega\mu_0(\sigma_{zx}E_x + \sigma_{zy}E_y + \sigma_{zz}E_z), \quad (9)$$

where μ is the air magnetic permeability and ω is the angular frequency. The staggered grid finite difference (SFD) scheme of Yee (1966) was used to discretize the electric fields, where the conductivity tensor is defined at the center of each cell. After grid discretization, we obtain the discrete system $\mathbf{S}\mathbf{e} = \mathbf{b}$ where \mathbf{e} is the unknown electric field vector, \mathbf{S} is a coefficient matrix, and \mathbf{b} is a vector related to the applied periodic boundary condition. The linear system of equations is solved on our shared-memory computer using the PARDISO direct solver (Alappat et al. 2020; Bollhöfer et al. 2019, 2020).

To validate our code, we first applied our code to the three 2-D classic models of Pek et al. (2008) illustrated in Marti (2014). The first model (left in Fig. 14a) is where the anisotropic 2-D body is buried within the two isotropic

layered Earth. Our 3-D anisotropic model (Fig. 1) is an adaptation of this model. The second model (middle in Fig. 14b) is the same as the first model, but the 2-D anisotropic body is extended to a greater depth. The last model (right in Fig. 14a) is where the top layer is anisotropic and lies on top of a 2-D isotropic body. Responses (Fig. 14b and c) from our code and from Marti (2014) for various values of vertical resistivity ρ_z are plotted as colored symbols, and colored lines, respectively.

Figure 14b and c shows that responses from our code and from Pek et al. (2008) perfectly lie on top of each other for all values of the vertical resistivity. Pek et al. (2008) claimed that they cannot see the influence of vertical resistivity in the first model as they used two low resistivity values. Here, we added one more case of $\rho_z = 500 \Omega\text{-m}$ to show that a slight deviation can be seen if a higher value of ρ_z is used.

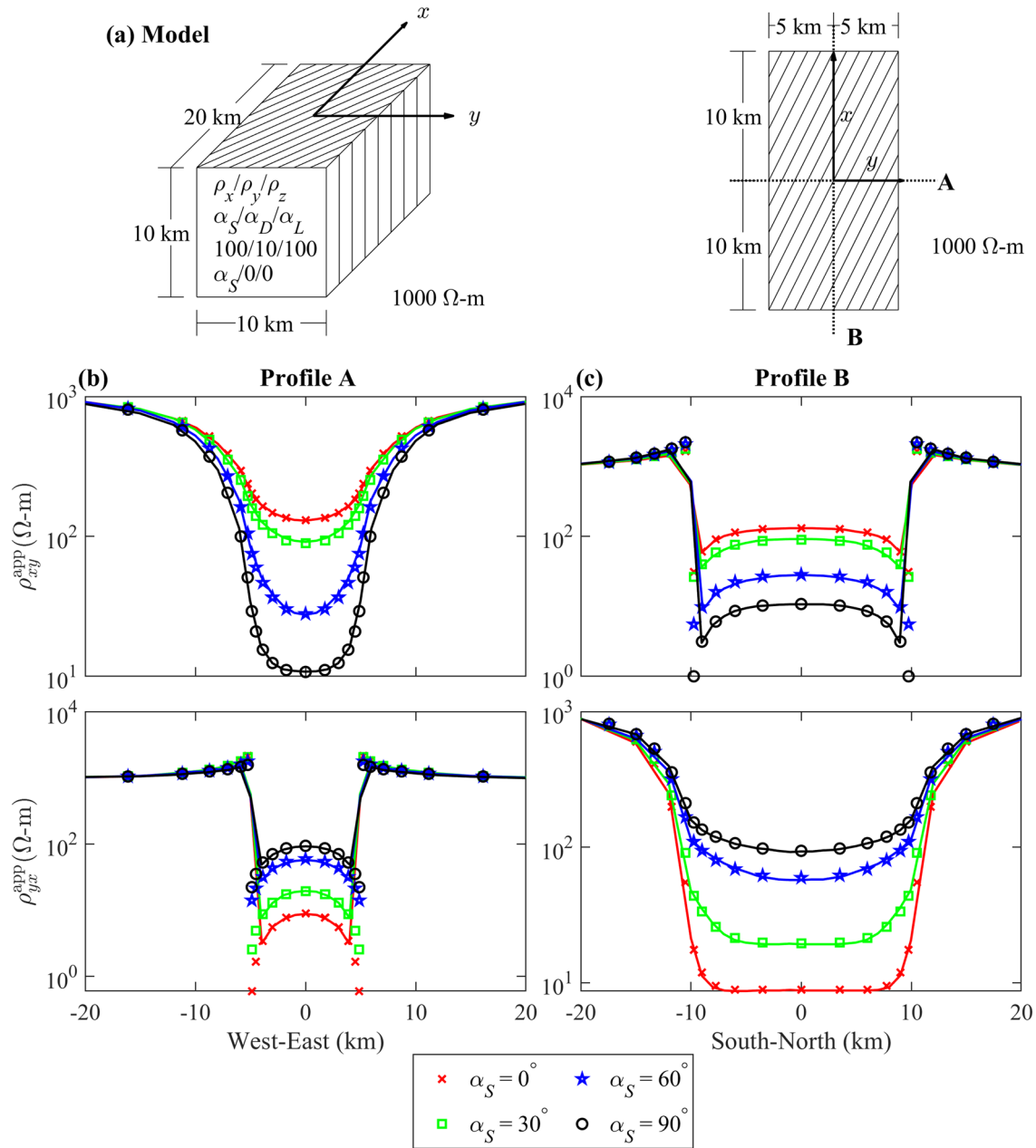


Fig. 16 **a** 3-D view and top view of the 3-D prism model of Han et al. (2018). **b** Apparent resistivities with various values of strike angles α_S along profile A, and **c** along profile B

Figure 15 shows examples of the apparent resistivities and magnitudes of the tipper at a period of 10 s computed from the model in Fig. 1 (a) from the iso50 model, (b) and (c) when ρ_x is 5 and 500 $\Omega\text{-m}$, respectively, and (d), (e), (f) and (g) when ρ_y and ρ_z are 5 and 500 $\Omega\text{-m}$, respectively, for the case of the axial anisotropy in section "The axial anisotropy". It is clear that ρ_x strongly affects the ρ_{xy}^{app} (or Z_{xy}), ρ_{yz}^{app} (or Z_{yz}) and $|T_y|$ (or T_y) responses since these responses greatly differ from those of the iso50 model. The effects of

ρ_y are the opposite to those of ρ_x . In contrast, all ρ_z cases are not different from those of the iso50 model indicating that ρ_z has a very weak effect on all of the responses.

Based on the governing Eqs. (7), (8) and (9), ρ_x and ρ_y are well connected to H_y and H_x , respectively. This is why ρ_x has a strong influence on the Z_{xy} , Z_{yz} and T_y responses, while ρ_y has strong influence on the Z_{yx} , Z_{xx} and T_x

responses. This helps to confirm that our numerical studies are correct.

We further validated our code on the 3-D prism model (Fig. 16a) used in Han et al. (2018). In this model, we varied the strike angle α_s and plotted the responses along profiles A and B (Fig. 16b and c). Our responses are in good agreement with the responses calculated from Han et al. (2018). The disagreement only occurs near the edges of the prism. We suspect that this might be due to our different grid discretization around the edges of the prism.

Appendix B: A condition for variations of the resistivity elements for the dipping anisotropic case

Evaluating $\mathbf{R}_x^T(\theta)\hat{\rho}\mathbf{R}_x(\theta)$ where the axial tensor

$$\hat{\rho} = \begin{bmatrix} \rho_x & 0 & 0 \\ 0 & \rho_y & 0 \\ 0 & 0 & \rho_z \end{bmatrix}, \text{ we obtain}$$

$$\mathbf{R}_x^T(\theta)\hat{\rho}\mathbf{R}_x(\theta) = \begin{bmatrix} \rho_x & 0 & 0 \\ 0 & \rho_y \cos^2 \theta + \rho_z \sin^2 \theta & (\rho_y - \rho_z) \cos \theta \sin \theta \\ 0 & (\rho_y - \rho_z) \cos \theta \sin \theta & \rho_z \cos^2 \theta + \rho_y \sin^2 \theta \end{bmatrix}$$

$$= \begin{bmatrix} \rho_{xx} & 0 & 0 \\ 0 & \rho_{yy} & \rho_{yz} \\ 0 & \rho_{zy} & \rho_{zz} \end{bmatrix}. \quad (10)$$

Our goal here is to vary each of ρ_{xx} , ρ_{yy} , ρ_{zz} and ρ_{yz} in order to see the effect on the surface responses. For example, we vary only ρ_{yz} , while keeping ρ_{xx} , ρ_{yy} , and ρ_{zz} constant, to see the influence of ρ_{yz} on \mathbf{Z} and \mathbf{T} . The variation of ρ_{yz} , or any of these elements, is invalid if $\begin{bmatrix} \rho_{xx} & 0 & 0 \\ 0 & \rho_{yy} & \rho_{yz} \\ 0 & \rho_{zy} & \rho_{zz} \end{bmatrix}$ cannot be reversed to $\mathbf{R}_x^T(\theta)\hat{\rho}\mathbf{R}_x(\theta)$ with reasonable θ and $\hat{\rho}$.

To make this process reversible, the equation linking ρ_x , ρ_y , and ρ_z to ρ_{xx} , ρ_{yy} , ρ_{zz} and ρ_{yz} elements is required to set up the conditions. This can be straightforwardly obtained by computing the determinant of the lower half 2×2 matrix of both right-hand side matrices of (10). This gives

$$\rho_{yy}\rho_{zz} - \rho_{yz}^2 = \rho_y\rho_z. \quad (11)$$

This way the θ angle is eliminated. Since all diagonal elements of both axial tensor (ρ_x , ρ_y , ρ_z) and dipping tensor (ρ_{xx} , ρ_{yy} , ρ_{zz}) must be positive, the reversible process can only be done if

$$\rho_{yy}\rho_{zz} - \rho_{yz}^2 > 0. \quad (12)$$

This is therefore the condition that must be satisfied while varying ρ_{yy} , ρ_{zz} , and ρ_{yz} . Note that as ρ_{xx} does not appear in (12), it can take on any positive value. In accordance with (12), ρ_{yy} or ρ_{zz} mostly have higher values, while $\rho_{yz} = \rho_{zy}$ can mostly be lower (or become a more conductive structure) relative to each other.

$$\text{For example, if } \mathbf{R}_x^T(45^\circ)\hat{\rho}\mathbf{R}_x(45^\circ) = \begin{bmatrix} 50 & 0 & 0 \\ 0 & 275 & 225 \\ 0 & 225 & 275 \end{bmatrix},$$

then from (12) we have $\rho_{yy} > \frac{\rho_{yz}^2}{\rho_{zz}} = 184$, and similarly for ρ_{zz} . We therefore can vary ρ_{yy} or ρ_{zz} in the range $(184, \infty)$ $\Omega\text{-m}$. For varying ρ_{yz} , the condition becomes $\rho_{yz}^2 < \rho_{yy}\rho_{zz} = 275^2$. Thus, ρ_{yz} can only be varied within the range $(0, 275)$ $\Omega\text{-m}$.

Acknowledgements

The authors would like to thank the Thailand Center of Excellence in Physics (ThEP) for funding to support WT throughout his Ph.D. study at Mahidol University, and also Dr. Michael Allen for editing the English of this manuscript.

Funding

Funding was provided by Thailand Center of Excellence in Physics (ThEP-61-PHM-MU1).

Author details

¹Department of Physics, Faculty of Science, Mahidol University, 272 Rama 6 Road, Rachatawee, Bangkok 10400, Thailand. ²Thailand Center of Excellence in Physics, Ministry of Higher Education, Science, Research and Innovation, 328 Si Ayutthaya Road, Bangkok 10400, Thailand. ³Curl-E Geophysics Co., Ltd., 85/87 Nantawan Village, Uttayan-Aksa Road, Salaya, Phuthamonthon District, Nakhon Pathom 73170, Thailand.

Received: 28 June 2022 Accepted: 30 December 2022

Published online: 26 January 2023

References

- Alappat C, Basermann A, Bishop AR, Fehske H, Hager G, Schenk O, Thies J, Wellein G (2020) A recursive algebraic coloring technique for hardware-efficient symmetric sparse matrix-vector multiplication. *ACM Trans Parallel Comput* 7(3):1. <https://doi.org/10.1145/3399732>
- Amatyakul P, Rung-Arunwan T, Siripunvaraporn W (2015) A pilot magnetotelluric survey for geothermal exploration in Mae Chan region, northern Thailand. *Geothermics* 55:31–38. <https://doi.org/10.1016/j.geothermics.2015.01.009>
- Amatyakul P, Boonchaisuk S, Rung-Arunwan T, Vachiriatienchai C, Wood SH, Pirarai K, Fuangwasdi A, Siripunvaraporn W (2016) Exploring the shallow geothermal fluid reservoir of Fang geothermal system, Thailand via a 3-D magnetotelluric survey. *Geothermics* 64:516–526. <https://doi.org/10.1016/j.geothermics.2016.08.003>
- Amatyakul P, Wood SH, Rung-Arunwan T, Vachiriatienchai C, Prommakorn N, Chanapiwat P, Siripunvaraporn W (2021) An assessment of a shallow geothermal reservoir of Mae Chan hot spring, northern Thailand via magnetotelluric surveys. *Geothermics*. <https://doi.org/10.1016/j.geothermics.2021.102137>
- Bai N, Zhou J, Hu X, Han B (2022) 3D edge-based and nodal finite element modeling of magnetotelluric in general anisotropic media. *Comput Geosci* 158:104975. <https://doi.org/10.1016/j.cageo.2021.104975>
- Bedrosian PA, Peacock JR, Dhary M, Sharif A, Feucht DW, Zahran H (2019) Crustal magmatism and anisotropy beneath the Arabian Shield—a cautionary tale. *J Geophys Res Solid Earth* 124(10):10153–10179. <https://doi.org/10.1029/2019JB017903>

- Bollhöfer M, Eftekhari A, Scheidegger S, Schenk O (2019) Large-scale sparse inverse covariance matrix estimation. *SIAM J Sci Comput* 41(1):A380–A401. <https://doi.org/10.1137/17m1147615>
- Bollhöfer M, Schenk O, Janalik R, Hamm S, Gullapalli K (2020) State-of-the-art sparse direct solvers. In: Grama A, Sameh AH (eds) *Parallel algorithms in computational science and engineering*. Springer, Cham, pp 3–33. https://doi.org/10.1007/978-3-030-43736-7_1
- Boonchaisuk S, Siripunvaraporn W, Ogawa Y (2013) Evidence for middle Triassic to Miocene dual subduction zones beneath the Shan-Thai terrane, western Thailand from magnetotelluric data. *Gondwana Res* 23(4):1607–1616. <https://doi.org/10.1016/j.jgr.2012.08.009>
- Cao H, Wang K, Wang T, Hua B (2018) Three-dimensional magnetotelluric axial anisotropic forward modeling and inversion. *J Appl Geophys* 153:75–89. <https://doi.org/10.1016/j.jappgeo.2018.04.015>
- Cao X, Huang X, Yin C, Yan L, Zhang B (2021) 3D MT anisotropic inversion based on unstructured finite-element method. *J Environ Eng Geophys* 26(1):49–60. <https://doi.org/10.32389/JEEG20-006>
- Comeau MJ, Becken M, Connolly JAD, Grayver AV, Kuvshinov AV (2020) Compaction-driven fluid localization as an explanation for lower crustal electrical conductors in an intracontinental setting. *Geophys Res Lett* 47(19):e2020GL088455. <https://doi.org/10.1029/2020GL088455>
- Feucht DW, Sheehan AF, Bedrosian PA (2017) Magnetotelluric imaging of lower crustal melt and lithospheric hydration in the Rocky Mountain Front Transition Zone, Colorado, USA. *J Geophys Res Solid Earth* 122(12):9489–9510. <https://doi.org/10.1002/2017JB014474>
- Feucht DW, Bedrosian PA, Sheehan AF (2019) Lithospheric signature of late Cenozoic extension in electrical resistivity structure of the Rio Grande Rift, New Mexico, USA. *J Geophys Res Solid Earth* 124(3):2331–2351. <https://doi.org/10.1029/2018JB016242>
- Guo Z, Egbert G, Dong H, Wei W (2020) Modular finite volume approach for 3D magnetotelluric modeling of the Earth medium with general anisotropy. *Phys Earth Planet Interiors* 309:106585. <https://doi.org/10.1016/j.pepi.2020.106585>
- Han B, Li Y, Li G (2018) 3D forward modeling of magnetotelluric fields in general anisotropic media and its numerical implementation in Julia. *Geophysics* 83(4):F29–F40. <https://doi.org/10.1190/geo2017-0515.1>
- Häuserer M, Junge A (2011) Electrical mantle anisotropy and crustal conductor: a 3-D conductivity model of the Rwenzori Region in western Uganda. *Geophys J Int* 185(3):1235–1242. <https://doi.org/10.1111/j.1365-246X.2011.05006.x>
- Jaysaval P, Shantsev DV, de la Kethulle de Ryhove S, Bratteland T (2016) Fully anisotropic 3-D EM modelling on a Lebedev grid with a multigrid preconditioner. *Geophys J Int* 207(3):1554–1572. <https://doi.org/10.1093/gji/ggw352>
- Kirkby A, Duan J (2019) Crustal structure of the Eastern Arunta Region, Central Australia, from magnetotelluric, seismic, and magnetic data. *J Geophys Res Solid Earth* 124(8):9395–9414. <https://doi.org/10.1029/2018JB016223>
- Kirkby A, Heinson G, Holford S (2016) The resistivity structure of the Penola Trough, Otway Basin from magnetotelluric data. *Aust J Earth Sci* 63(5):571–582. <https://doi.org/10.1080/08120099.2016.1232311>
- Kong W, Lin C, Tan H, Peng M, Tong T, Wang M (2018) The effects of 3d electrical anisotropy on magnetotelluric responses: synthetic case studies. *J Environ Eng Geophys* 23(1):61–75. <https://doi.org/10.2113/JEEG23.1.61>
- Kong W, Tan H, Lin C, Unsworth M, Lee B, Peng M, Wang M, Tong T (2021) Three-dimensional inversion of magnetotelluric data for a resistivity model with arbitrary anisotropy. *J Geophys Res Solid Earth* 126(8):e2020JB020562. <https://doi.org/10.1029/2020JB020562>
- Liddell M, Unsworth M, Pek J (2016) Magnetotelluric imaging of anisotropic crust near Fort McMurray, Alberta: implications for engineered geothermal system development. *Geophys J Int* 205(3):1365–1381. <https://doi.org/10.1093/gji/ggw089>
- Liu Y, Xu Z, Li Y (2018) Adaptive finite element modelling of three-dimensional magnetotelluric fields in general anisotropic media. *J Appl Geophys* 151:113–124. <https://doi.org/10.1016/j.jappgeo.2018.01.012>
- Liu Y, Junge A, Yang B, Löwer A, Cembrowski M, Xu Y (2019) Electrically anisotropic crust from three-dimensional magnetotelluric modeling in the Western Junggar, NW China. *J Geophys Res Solid Earth* 124(9):9474–9494. <https://doi.org/10.1029/2019JB017605>
- Löwer A, Junge A (2017) Magnetotelluric transfer functions: phase tensor and tipper vector above a simple anisotropic three-dimensional conductivity anomaly and implications for 3D isotropic inversion. *Pure Appl Geophys* 174(5):2089–2101. <https://doi.org/10.1007/s00024-016-1444-3>
- Luo W, Wang K, Cao H, Duan C, Wang T, Jian X (2020) Joint inversion of magnetotelluric impedance and tipper data in 3D axial anisotropic media. *J Environ Eng Geophys* 25(1):25–36. <https://doi.org/10.2113/jeeeg19-022>
- Mandolesi E, Jones AG (2012) Magnetotelluric Inversion in a 2D Anisotropic Environment. Paper presented at the EGU General Assembly Conference Abstracts, April 01, 2012, pp 13561
- Martí A (2014) The role of electrical anisotropy in magnetotelluric responses: from modelling and dimensionality analysis to inversion and interpretation. *Surv Geophys* 35(1):179–218. <https://doi.org/10.1007/s10712-013-9233-3>
- Matsuno T, Evans RL (2017) Constraints on lithospheric mantle and crustal anisotropy in the NoMelt area from an analysis of long-period seafloor magnetotelluric data. *Earth Planets Space* 69(1):138. <https://doi.org/10.1186/s40623-017-0724-1>
- Matsuno T, Baba K, Utada H (2020) Probing 1-D electrical anisotropy in the oceanic upper mantle from seafloor magnetotelluric array data. *Geophys J Int* 222(3):1502–1525. <https://doi.org/10.1093/gji/ggaa221>
- Miensopust MP, Jones AG (2011) Artefacts of isotropic inversion applied to magnetotelluric data from an anisotropic Earth. *Geophys J Int* 187(2):677–689. <https://doi.org/10.1111/j.1365-246X.2011.05157.x>
- Miller RV, Meju MA, Saleh AS, Mackie RL, Miorelli F (2019) Structure-guided 3D joint inversion of CSEM and MT data from a fold-thrust belt. In: SEG Technical Program Expanded Abstracts 2019. SEG Technical Program Expanded Abstracts. Society of Exploration Geophysicists, pp 1115–1119. <https://doi.org/10.1190/segam2019-3216157.1>
- Pek J, Santos FAM (2002) Magnetotelluric impedances and parametric sensitivities for 1-D anisotropic layered media. *Comput Geosci* 28(8):939–950. [https://doi.org/10.1016/S0098-3004\(02\)00014-6](https://doi.org/10.1016/S0098-3004(02)00014-6)
- Pek J, Santos FAM (2006) Magnetotelluric inversion for anisotropic conductivities in layered media. *Phys Earth Planet Inter* 158(2):139–158. <https://doi.org/10.1016/j.pepi.2006.03.023>
- Pek J, Santos FAM, Li Y (2008) Anomalies of magnetotellurics field due to electrical anisotropy and their inverse conductivity images. 19 EM Induction Workshop, Beijing, China
- Rivera-Rios AM, Zhou B, Heinson G, Krieger L (2019) Multi-order vector finite element modeling of 3D magnetotelluric data including complex geometry and anisotropy. *Earth, Planets Space* 71(1):92. <https://doi.org/10.1186/s40623-019-1071-1>
- Rong Z, Liu Y, Yin C, Wang L, Ma X, Qiu C, Zhang B, Ren X, Su Y, Weng A (2022) Three-dimensional magnetotelluric inversion for arbitrarily anisotropic earth using unstructured tetrahedral discretization. *J Geophys Res Solid Earth* 127(8):e2021JB023778. <https://doi.org/10.1029/2021JB023778>
- Rung-Arunwan T, Siripunvaraporn W, Utada H (2016) On the Berdichevsky average. *Phys Earth Planet Inter* 253:1–4
- Segovia MJ, Diaz D, Slezak K, Zuñiga F (2021) Magnetotelluric study in the Los Lagos Region (Chile) to investigate volcano-tectonic processes in the Southern Andes. *Earth Planets Space* 73(1):5. <https://doi.org/10.1186/s40623-020-01332-w>
- Siripunvaraporn W (2012) Three-dimensional magnetotelluric inversion: an introductory guide for developers and users. *Surv Geophys* 33(1):5–27. <https://doi.org/10.1007/s10712-011-9122-6>
- Siripunvaraporn W, Egbert G (2000) An efficient data-subspace inversion method for 2-D magnetotelluric data. *Geophysics* 65(3):791–803
- Siripunvaraporn W, Egbert G (2002) Numerical accuracy of magnetotelluric modeling: a comparison of finite difference approximations. *Earth Planets Space* 54(6):721–725
- Siripunvaraporn W, Egbert G (2009) WSINV3DMT: Vertical magnetic field transfer function inversion and parallel implementation. *Phys Earth Planet Inter* 173(3):317–329. <https://doi.org/10.1016/j.pepi.2009.01.013>
- Siripunvaraporn W, Sarakorn W (2011) An efficient data space conjugate gradient Occam's method for three-dimensional magnetotelluric inversion. *Geophys J Int* 186(2):567–579. <https://doi.org/10.1111/j.1365-246X.2011.05079.x>
- Siripunvaraporn W, Egbert G, Lenbury Y, Uyeshima M (2005) Three-dimensional magnetotelluric inversion: data-space method. *Phys Earth Planet Inter* 150(1):3–14. <https://doi.org/10.1016/j.pepi.2004.08.023>
- Wang L, Hitchman AP, Ogawa Y, Siripunvaraporn W, Ichiki M, Fuji-ta K (2014) A 3-D conductivity model of the Australian continent using observatory

- and magnetometer array data. *Geophys J Int* 198(2):1143–1158. <https://doi.org/10.1093/gji/ggu188>
- Wang T, Wang K-P, Tan H-D (2017) Forward modeling and inversion of tensor CSAMT in 3D anisotropic media. *Appl Geophys* 14(4):590–605. <https://doi.org/10.1007/s11770-017-0644-7>
- Xiao T, Huang X, Wang Y (2019) 3D MT modeling using the T- Ω method in general anisotropic media. *J Appl Geophys* 160:171–182. <https://doi.org/10.1016/j.jappgeo.2018.11.012>
- Ye G, Unsworth M, Wei W, Jin S, Liu Z (2019) The lithospheric structure of the Solonker Suture zone and adjacent areas: crustal anisotropy revealed by a high-resolution magnetotelluric study. *J Geophys Res Solid Earth* 124(2):1142–1163. <https://doi.org/10.1029/2018JB015719>
- Ye Y, Du J, Liu Y, Ai Z, Jiang F (2021) Three-dimensional magnetotelluric modeling in general anisotropic media using nodal-based unstructured finite element method. *Comput Geosci* 148:104686. <https://doi.org/10.1016/j.cageo.2021.104686>
- Yee K (1966) Numerical solution of initial boundary value problems involving Maxwell's equations in isotropic media. *IEEE Trans Antennas Propag* 14(3):302–307. <https://doi.org/10.1109/TAP.1966.1138693>
- Yin C (2003) Inherent nonuniqueness in magnetotelluric inversion for 1D anisotropic models. *Geophysics* 68(1):138–146. <https://doi.org/10.1190/1.1543201>
- Yu G, Xiao Q, Zhao G, Li M (2018) Three-dimensional magnetotelluric responses for arbitrary electrically anisotropic media and a practical application. *Geophys Prospect* 66(9):1764–1783. <https://doi.org/10.1111/1365-2478.12690>

Publisher's Note

Springer Nature remains neutral with regard to jurisdictional claims in published maps and institutional affiliations.

Submit your manuscript to a SpringerOpen[®] journal and benefit from:

- Convenient online submission
- Rigorous peer review
- Open access: articles freely available online
- High visibility within the field
- Retaining the copyright to your article

Submit your next manuscript at ► [springeropen.com](https://www.springeropen.com)